OPEN BIOLOGY

royalsocietypublishing.org/journal/rsob

Research

Cite this article: Molton O, Bignucolo O, Kellenberger S. 2024 Identification of the modulatory Ca^{2+}-binding sites of acid-sensing ion channel 1a. *Open Biol.* **14**: 240028.
https://doi.org/10.1098/rsob.240028

Received: 2 February 2024
Accepted: 28 April 2024

Subject Areas:
neuroscience, cellular biology, bioinformatics

Keywords:
acid-sensing ion channel, ion channel, activation, pH dependence, molecular dynamics simulations

Author for correspondence:
Stephan Kellenberger
e-mail: stephan.kellenberger@unil.ch

Electronic supplementary material is available online at https://doi.org/10.6084/m9.figshare.c.7227186.

THE ROYAL SOCIETY PUBLISHING

Identification of the modulatory Ca^{2+}-binding sites of acid-sensing ion channel 1a

Ophélie Molton[1], Olivier Bignucolo[2] and Stephan Kellenberger[1]

[1]Department of Biomedical Sciences, University of Lausanne, 1011 Lausanne, Switzerland
[2]Swiss Institute of Bioinformatics, 4056 Basel, Switzerland

SK, 0000-0003-1755-6198

Acid-sensing ion channels (ASICs) are neuronal Na^+-permeable ion channels activated by extracellular acidification. ASICs are involved in learning, fear sensing, pain sensation and neurodegeneration. Increasing the extracellular Ca^{2+} concentration decreases the H^+ sensitivity of ASIC1a, suggesting a competition for binding sites between H^+ and Ca^{2+} ions. Here, we predicted candidate residues for Ca^{2+} binding on ASIC1a, based on available structural information and our molecular dynamics simulations. With functional measurements, we identified several residues in cavities previously associated with pH-dependent gating, whose mutation reduced the modulation by extracellular Ca^{2+} of the ASIC1a pH dependence of activation and desensitization. This occurred probably owing to a disruption of Ca^{2+} binding. Our results link one of the two predicted Ca^{2+}-binding sites in each ASIC1a acidic pocket to the modulation of channel activation. Mg^{2+} regulates ASICs in a similar way as does Ca^{2+}. We show that Mg^{2+} shares some of the binding sites with Ca^{2+}. Finally, we provide evidence that some of the ASIC1a Ca^{2+}-binding sites are functionally conserved in the splice variant ASIC1b. Our identification of divalent cation-binding sites in ASIC1a shows how Ca^{2+} affects ASIC1a gating, elucidating a regulatory mechanism present in many ion channels.

1. Introduction

Acid-sensing ion channels (ASICs) are H^+-gated and Na^+-permeable ion channels widely expressed in the nervous system [1,2]. They are involved in learning, fear sensing, pain sensation and neurodegeneration after ischaemia [1–3]. Four ASIC genes encode six different subunits in rodents. Functional ASICs assemble into heterotrimeric and homotrimeric channels whose pH dependence and current kinetics depend on the subunit composition. ASIC1a is the most pH-sensitive subunit in the central nervous system [1,2]. The shape of each subunit resembles a hand holding a small ball with the different domains labelled palm, knuckle, finger, thumb and β-ball ([4]; figure 1*a*). The channel contains several electronegative vestibules to which some pharmacological ligands bind, such as the acidic pocket and the central vestibule. Each acidic pocket is enclosed by the thumb, finger and β-ball domains of one subunit and the palm of an adjacent subunit; the central vestibule is located in the palm region [4–6].

Extracellular free Ca^{2+} concentrations decrease locally during high neuronal activity, during seizures and in ischaemic stroke [7–9]. Lowering the Ca^{2+} concentration affects the activity of many neuronal ion channels [10–12] and thereby neuronal excitability [13]. Extracellular acidification induces a transient opening of ASICs, followed by a current decay owing to the entry into a non-conducting desensitized state (figure 1*b*,*c*) [14]. Calcium ions appear to compete with protons for binding sites in ASICs since an increase in

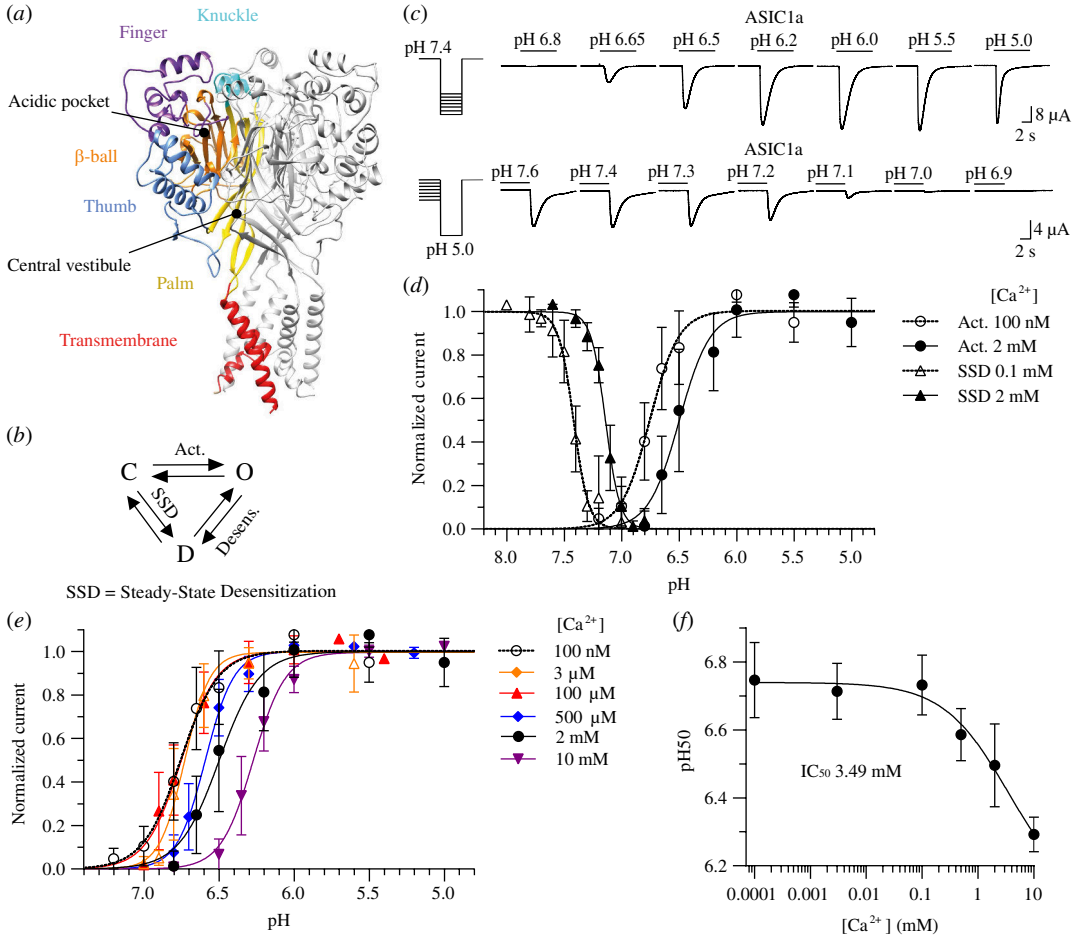

Figure 1. Calcium modulates the pH dependence of activation and steady-state desensitization (SSD) of ASIC1a. (*a*) Structural image of ASIC1a trimer, based on a model of the crystal structure (PDB code 5WKU). The different domains are indicated by specific colours in one of the three ASIC subunits. (*b*) Kinetic scheme of ASIC1a showing the three functional states (closed (C), open (O) and desensitized (D)) and the transitions between these states. Act., activation; Desens., desensitization. (*c*) Representative current traces of *Xenopus laevis* oocytes expressing ASIC1a wild-type were obtained by two-electrode voltage clamp to −60 mV to determine the pH dependence of activation and the pH dependence of SSD. Channels were activated every 60 s by a 10 s perfusion with stimulation solution. For the measurement of the activation pH dependence, stimulation solutions of varying pH were applied, and the pH of the conditioning solution perfused between stimulations was 7.4. For the measurement of the SSD pH dependence, solutions of varying pH were applied for 50 s before the stimulation by pH 5.0. (*d*) pH dependence curves of activation and SSD. Activation curves were measured at 100 nM free Ca^{2+} (open circles) or 2 mM Ca^{2+} in the stimulation solution (filled circles) with a conditioning solution containing 2 mM Ca^{2+}. SSD curves were measured at 0.1 mM Ca^{2+} (open triangles) or 2 mM Ca^{2+} in the conditioning solution (filled triangles), with 2 mM Ca^{2+} in the stimulation solution. Currents were normalized to the maximal peak current. The lines represent fits to the Hill equation ($n = 17–56$). (*e*) pH dependence curves of activation measured at the indicated Ca^{2+} concentrations. Currents were normalized to the maximal peak current. The lines represent fits to the Hill equation ($n = 9–56$). (*f*) Plot of the pH_{50} as a function of the Ca^{2+} concentrations, based on (*e*). The lines represent fits to an inhibition equation. (*d–f*) Data are shown as mean ± s.d.

their concentration shifts the pH dependence towards more acidic pH values [15,16]. In addition to its effects on gating, extracellular Ca^{2+} also inhibits ASIC1a currents by a pore block owing to binding into the ion pore, with an IC_{50} of the order of millimolar [17]. In ASIC3, two different Ca^{2+}-binding sites are involved in channel regulation, one in the pore and one in the acidic pocket [18,19]. For ASIC1a, the understanding of gating modulation by Ca^{2+} remains incomplete because the Ca^{2+}-binding sites mediating the shift of its pH dependence have not been identified yet.

A recent study showed approximate locations of Ca^{2+} binding in the acidic pocket and central vestibule of chicken ASIC1a, based on crystals that were soaked in Ba^{2+} [20]. These two cavities had been shown to contain numerous proton binding sites [21–25] and to undergo substantial conformational changes during gating [6,26–30]. In the high-pH resting-state structure, two divalent ions bind to each acidic pocket, while three divalent ions bind to the central vestibule. In the low-pH desensitized state, the divalent cation binding sites in the central vestibule are lost and the number of binding sites in each acidic pocket is reduced from two to one [20].

Here, we have carried out molecular dynamics (MD) simulations to refine the Ca^{2+} coordination in an ASIC1a structural model, identifying, out of the many negatively charged residues, specific residues in the acidic pocket and the central vestibule as the most likely Ca^{2+}-binding sites. We then mutated candidate residues and compared the Ca^{2+} modulation of the pH dependence of wild-type (WT) and mutant channels. This identified several residues in the acidic pocket, the central vestibule and the pore entry that contribute to the modulatory effect of Ca^{2+} and are most likely part of Ca^{2+}-binding sites. In addition, we show that Mg^{2+} shares binding sites with Ca^{2+} for desensitization and that Ca^{2+}-binding sites for desensitization in the central vestibule are functionally conserved between the splice variants ASIC1a and ASIC1b.

2. Results

(a) Calcium modulates ASIC1a function

To investigate the effects of Ca^{2+} on ASIC1a activity, the pH dependence of activation and steady-state desensitization (SSD) were measured at two different extracellular Ca^{2+} concentrations. WT or mutant ASIC1a channels were expressed in *Xenopus laevis* oocytes, and their function was measured by a two-electrode voltage clamp. To determine the pH dependence of activation ('Act.' in figure 1*b–d*), the channels were exposed for 10 s, once per minute, to a stimulation solution, testing thereby the current response to a series of increasingly acidic pH solutions (figure 1*c*). The conditioning pH between stimulations was 7.4 in all experiments unless noted. The Ca^{2+} concentration was kept at 2 mM in the conditioning solution, while it was either 2 mM or 100 nM in the stimulation solution. In figure 1*d*, normalized currents measured with this protocol are plotted as spheres as a function of the stimulation pH. Decreasing the extracellular Ca^{2+} concentration shifted the pH dependence to more alkaline values. Fitting the pH dependence curves yielded pH values of half-maximal activation (pH_{50}) of 6.50 ± 0.12 (n = 50) at 2 mM Ca^{2+} and 6.75 ± 0.11 (n = 50) at 100 nM Ca^{2+}, indicating a shift towards more alkaline pH_{50} values by 0.25 pH units with the lower Ca^{2+} concentration. The pH dependence of SSD, the transition from the closed to the desensitized state without apparent opening (figure 1*b*), was measured by a 10 s stimulation by pH 5.0 once per minute, which was preceded by 50 s exposures to conditioning solutions of increasingly acidic pH (figure 1*c*). This protocol measures the channel availability for activation after exposure to the indicated conditioning pH. The Ca^{2+} concentration was either 2 mM or 0.1 mM in the conditioning solutions and was kept constant at 2 mM in the stimulation solution. Normalized current amplitudes are plotted as triangles as a function of the conditioning pH in figure 1*d*. The pH of half-maximum desensitization (pHD_{50}) was 7.14 ± 0.04 (n = 17) at 2 mM Ca^{2+} and 7.42 ± 0.06 (n = 17) at 0.1 mM Ca^{2+}, indicating a shift towards more alkaline pHD_{50} values by 0.28 pH units with the lower Ca^{2+} concentration. Thus, lowering the Ca^{2+} concentration shifts the ASIC1a pH dependence of activation and SSD to more alkaline values, as previously shown [15]. The pH dependence of activation was measured at additional Ca^{2+} concentrations to determine the apparent Ca^{2+} affinity of the regulatory Ca^{2+} binding (figure 1*e*). A plot of the pH_{50} values as a function of the Ca^{2+} concentration in the stimulation solutions yielded an IC_{50} of 3.5 mM (figure 1*f*).

(b) Prediction of candidates for Ca^{2+} coordination by molecular dynamics simulations

The twofold positively charged Ca^{2+} ions tend to bind to negatively charged residues that contain carboxylate groups. To obtain a more precise prediction of divalent-coordinating residues than provided by the structure of the Ba^{2+}-soaked crystals [20] and identify residues participating in the coordination of divalent cations, MD simulations were carried out with a human ASIC1a model of the chicken ASIC1a resting structure (PDB code 6VTL) [26], in which two Ca^{2+} ions per acidic pocket and a total of three Ca^{2+} ions in the central vestibule were placed according to their approximate published location [20]. The protonation state of the titratable side chains was updated every 100 ns to mimic pH 7.4 (Material and methods) during the MD simulations that were carried out for 600 ns using a system containing two independent channels. During these simulations, the proximity of the Ca^{2+} ions to acidic residues (Asp and Glu) was monitored, and the residues interacting (i.e. Ca^{2+}-side-chain distance < 6 Å) during at least 10% of each period of 100 ns were included in a more detailed analysis (Material and methods).

Sixteen residues per subunit fulfilled this criterion: 12 in the acidic pocket and four in the central vestibule. Of these residues, Ca^{2+}-side-chain distances (distance between the centre of the Ca^{2+} atom and the gravity centre of the two oxygen residues of the carbonyl group) were measured every 400 ps. Figure 2*a* plots for each residue the fraction of time at which the distance to the closest Ca^{2+} ion was < 4 or < 6 Å, respectively. Figure 2*b* shows the mean distance of a given residue to the closest Ca^{2+} ion. For this analysis, only Ca^{2+}-side-chain distances ≤10 Å were considered. Residues that had, during ≥ 50% of the simulation time, a Ca^{2+} ion in their proximity displayed relatively short (approx. 5 Å) distances to the closest Ca^{2+} ion. This analysis predicted E97, E219, E238, E242, D347, D351 and D409 of the acidic pocket and E375, E413 and E418 of the central vestibule as good candidates for Ca^{2+} binding and D237 and E355 (acidic pocket) and E79 (central vestibule) as lower priority candidates (figure 2*a,b*). The location in the structure of these residues is shown in figure 2*c,d*. Residues facing the external part of the protein or being distant from other acidic residues, such as E177, showed lower Ca^{2+} interactions in the MD simulations and were therefore not functionally investigated.

Besides guiding the choice of residues of interest for the functional analysis, the MD simulations provided information on the dynamics of Ca^{2+} binding in both the acidic pocket and the central vestibule. Since the simulations were carried out in two separate ASIC channels, they provided information on the dynamics of six acidic pockets with two Ca^{2+} ions each and six subunit-Ca^{2+} ion pairs of the central vestibule. In the acidic pocket, the Ca^{2+} ion placed at the beginning of the simulation close to E219 and D409, which we name here the 'inner AP Ca^{2+} site', stayed in 4 out of 6 simulations throughout the entire simulation in close proximity of E219, D409 and generally, at an increased distance, to E242, as illustrated for a typical simulation in figure 2*e*. In the two other simulations, the Ca^{2+} moved towards residues D351 and D347 and left the acidic pocket after about 300 ns. The second Ca^{2+} ion was placed in proximity of E97, named here 'outer AP Ca^{2+} site'. In 5 out of 6 simulations, it moved during the simulation towards the centre of the acidic pocket into proximity of D347 and D351, or E238, where it stayed for the rest of the simulation (figure 2*f,g*). In one simulation, the Ca^{2+} ion stayed throughout the simulation close to E97.

In the central vestibule, the Ca^{2+} ion close to a given subunit changed frequently in two simulations positions relative to E79, E375, E413 and E418, without showing any preference for a given residue. In two simulations, it stayed for most of the time close to E375 and E413, as illustrated in figure 2*h*. In two simulations, the Ca^{2+} ion stayed for approximately 400 ns close to E375 and E413 and in part to E418, before switching its position with the Ca^{2+} ion initially positioned close to the adjacent subunit (electronic supplementary material, figure S1).

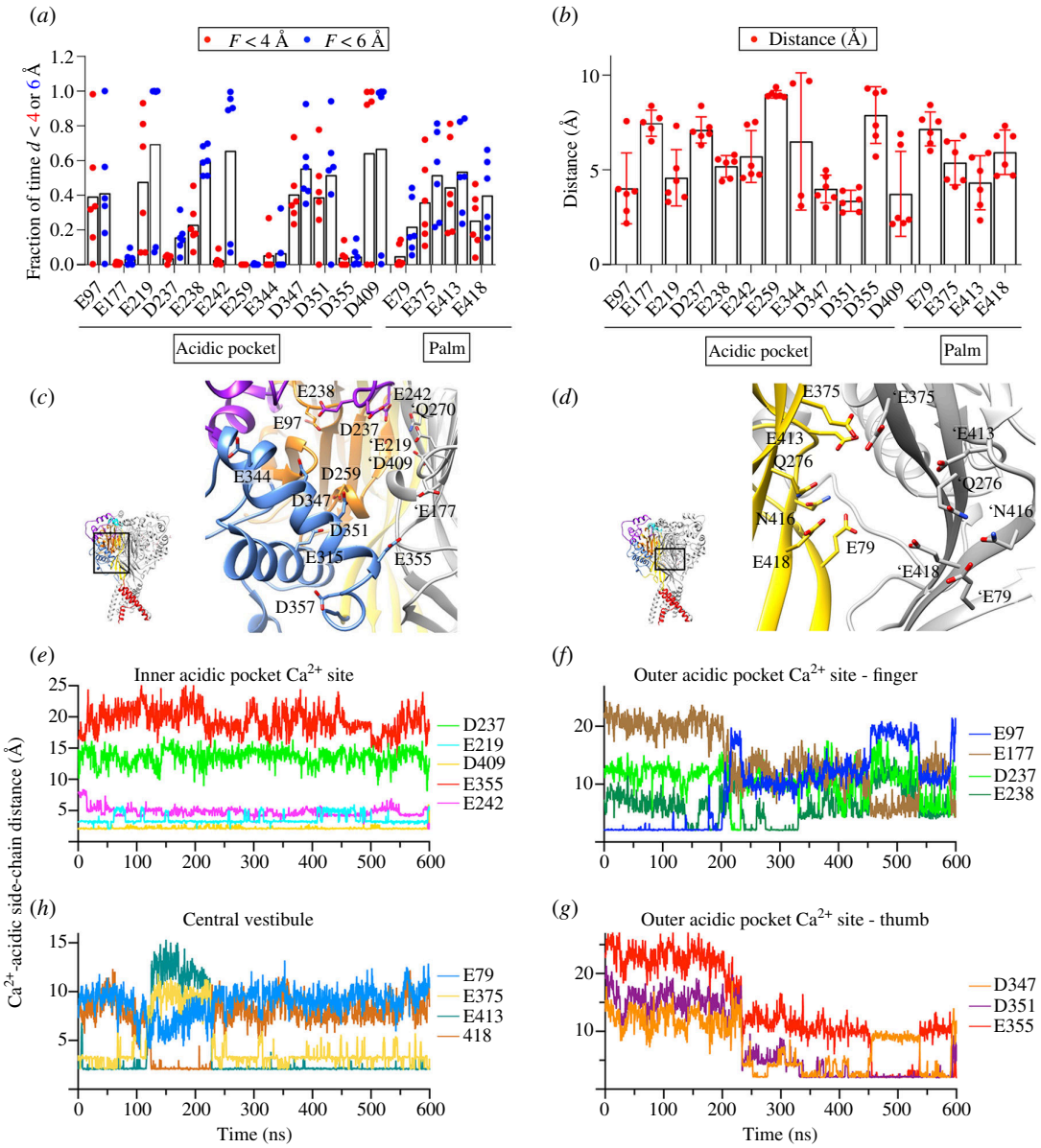

Figure 2. MD simulations predict Ca^{2+}-binding residues. MD simulations were carried out over a total duration of 600 ns with two independent ASIC1a channels, containing thus six acidic pockets (APs) with two Ca^{2+} ions each and six subunit-Ca^{2+} pairs in the central vestibule (Material and methods). Distances between Ca^{2+} ions and the centre-of-mass of the carbonyl groups of acidic side chains were measured, and candidate binding residues were ranked and selected as described in Material and methods. (*a*) Fraction of time during which a Ca^{2+} ion was closer than 4 Å (red symbols) or 6 Å (blue symbols) to the indicated residue. (*b*) Distance between Ca^{2+} ions and the centre-of-mass of the carbonyl groups of acidic side chains. For this analysis, distances >10 Å were excluded. (*a*,*b*) Each data point represents the measurement of a different AP or a different central vestibule subunit-Ca^{2+} ion pair. (*c*,*d*) Structural images of the AP (*c*) and the central vestibule (*d*) in the closed conformation (model based on PDB 5WKU), showing the residues for which distances to Ca^{2+} ions were measured in (*a*,*b*). Additional residues, not included in the MD analysis but studied by functional experiments, are shown: Q270 (close to E219 and E242 (*c*)) and Q276 and N416 (close to E413 and E418 for Q276 and E79 for N416 (*d*)). Amino acid residue labels without prefixes and labels with the prefix (') are on different subunits. In (*d*), only two subunits are shown. (*e*–*h*) Time course of Ca^{2+}-side-chain distances for two Ca^{2+} ions in the same AP, one placed at the inner AP Ca^{2+} site (*e*) and one placed at the outer AP Ca^{2+} site, with distances to finger (*f*) and thumb residues (*g*)), and of a Ca^{2+} ion placed in the central vestibule (*h*). These are representative traces out of six measurements each in the AP and for Ca^{2+} ion central vestibule subunit pairs.

(c) Mutations in the acidic pocket and the central vestibule decrease the effect of Ca^{2+} on ASIC1a activation

Thirteen negatively charged residues were selected as candidate residues for Ca^{2+} binding sites of ASIC1a based on the MD simulations and their position in the ASIC1a structure. In addition, two Gln and one Asn were included as candidates for Ca^{2+}-binding sites, since they are in proximity of some candidates identified by MD simulations and could interact with Ca^{2+} ions with their partial negative charge (figure 2*c*,*d*). These residues were mutated individually to Ala. Alterations of the charge and size of side chains by the mutation to Ala should decrease the ability of Ca^{2+} to bind and compromise its effect on the ASIC1a pH dependence in case the mutated residue is part of a Ca^{2+}-binding site. The pH dependence was determined in the same oocyte at two Ca^{2+} concentrations, 2 mM and 100 nM. At 2 mM Ca^{2+}, the pH_{50} values of many mutants were significantly lower than the WT values (figure 3*a*,*b*), indicating a decreased pH sensitivity. The ASIC1a WT ΔpH_{50}, measured as $pH_{50,100\ nM}$–$pH_{50,2\ mM}$, was 0.25 ± 0.09 (n = 50; figure 3*c*). In the acidic pocket, the mutations E219A, E238A, Q270A and D347A decreased the ΔpH_{50} significantly by 38–48%, compared with the WT (figure 3*c*). A channel construct containing these four mutations,

termed 'AP-Act', showed a significant decrease of the ΔpH_{50} compared with the WT (0.10 ± 0.09, n = 8; figure 3*d*), highlighting the importance of these four residues for binding Ca^{2+} in the acidic pocket. The mutant D409A showed a significant increase of the ΔpH_{50} compared with the WT (0.41 ± 0.09, n = 10; figure 3*c*), suggesting that this residue does not favour Ca^{2+} coordination or the competition with protons in the context of activation. In the central vestibule, the mutants E79A and E418A showed the strongest deviation from WT, displaying no significant modulation of the pH_{50} by Ca^{2+} (figure 3*a–c*). In addition, the mutations Q276A, E375A and E413A decreased the ΔpH_{50} significantly by 38–63% (figure 3*c*). These effects were significantly smaller than the decrease in ΔpH_{50} induced by the mutation E79A (Q276A, $p < 0.01$; E375A, $p < 0.0001$; E413A, $p < 0.001$; ANOVA and Tukey's multiple comparisons test).

A channel containing these five mutations of the central vestibule that individually had produced a significant reduction of the ΔpH_{50}, 'CV-Act', had only a sustained current (traces in figure 3*e*), although individual mutations except for Q276A and E79A had not induced any sustained currents. In addition, the pH dependence was strongly shifted towards acidic values (figure 3*b*). The CV-Act mutant showed no significant difference in the Ca^{2+}-dependent ΔpH_{50} compared with the WT (0.28 ± 0.25, n = 7; figure 3*d*). The lack of desensitization and the reduced pH sensitivity highlight the important role of these five residues for desensitization. On a construct combining the four acidic pocket and five central vestibule mutations, termed 'AP+CV-Act', the modulation by Ca^{2+} was variable and not significantly different from WT (ΔpH_{50} = 0.14 ± 0.16, n = 7). The currents of this mutant were mostly sustained, showing only a very weak desensitization in the 2 mM Ca^{2+} condition (figure 3*e*). We had previously observed sustained currents and strongly shifted pH dependence when mutations of the palm/central vestibule were combined [27], suggesting that these combined mutants were open to an alternative open state. Since the basic current properties of the CV-Act and AP + CV-Act mutants are profoundly different from the WT, they cannot be used to infer how the combination of mutations would affect the default opening process of ASIC1a. Although the combination of central vestibule mutations was not conclusive, the analysis of the activation shows that four mutations in the acidic pocket and five mutations in the central vestibule decrease the Ca^{2+}-dependent ΔpH_{50} compared with the WT.

(d) Molecular dynamics simulations with ASIC1a carrying mutations in the acidic pocket show shorter residency times of Ca^{2+} ions

To study Ca^{2+} ion dynamics in a channel lacking Ca^{2+}-binding sites in the acidic pocket, MD simulations with the combined mutant 'AP-Act' were carried out, and the same analysis as for the simulations with ASIC1a WT was applied. The fraction of time at which the distance of a residue to the closest Ca^{2+} ion was <4 Å or <6 Å showed similar results in the AP-Act mutant (electronic supplementary material, figure S2*a*) as for the WT (figure 2*a*). Also, the mean distance of a given residue to the closest Ca^{2+} ion was not different between AP-Act and the WT, except for E355 for which the distance was shorter in the mutant (electronic supplementary material, figure S2*b*). Note that the mean distance measurement included only Ca^{2+} ions that were not farther away than 10 Å from the residue. The inspection of the trajectories showed that for the outer AP Ca^{2+} site, Ca^{2+} ions of the AP-Act mutant stayed close to the residues E97 and D237 until approximately 150 ns, before moving and getting closer to E177, D351 and E355 (figure 3*f*), similarly to the observations with the WT (figure 2*f,g*). Unlike the WT where the Ca^{2+} ion placed in the outer AP Ca^{2+} site remained in the acidic pocket until the end of the simulation in 6 out of 6 simulations, it left the mutant acidic pocket during the 500 ns simulations in 5 out of 6 simulations. Thus, the absence of residues E238 and D347 appears to destabilize the interaction of Ca^{2+} ions with the acidic pocket, supporting the conclusion that these two residues are critically involved in the Ca^{2+}-binding site. For the inner AP Ca^{2+} site, the Ca^{2+} ion remained close to D409 and E242 throughout the simulation in all six simulations (electronic supplementary material, figure S2*c*). However, a high variability in the measured distances was observed during the simulations, suggesting instability of Ca^{2+} ions at this site in the absence of E219 and Q270. As a means of a more quantitative analysis of the presence of Ca^{2+} ions in the acidic pocket, the fraction of time at which the distance of a residue to the closest Ca^{2+} ion was <20 Å was measured (figure 3*g*). Ca^{2+} ions in AP-Act showed a tendency to spend less time close to the acidic pocket residues E97, E177 and D351 compared with the WT. This probability was significantly lower for E355 in mutant compared with WT ASIC1a. Taken together, the MD simulations suggest that the absence of the E219, E238, Q270 and D347 side chains destabilizes mostly the outer AP Ca^{2+}-binding site.

(e) Acidic pocket and central vestibule mutations decrease the Ca^{2+} modulation of steady-state desensitization

The pHD_{50} values of SSD of many mutants were also significantly different from WT (figure 4*a,b*). A significantly decreased ΔpHD_{50} compared with WT (0.28 ± 0.03; n = 17) was observed for the seven acidic pocket mutants, E97A, E219A, E238A, E242A, Q270A, D347A and D409A (figure 4*c*). The ΔpHD_{50} was decreased by these mutations by 14–32%. In the central vestibule, only the mutants E375A and E413A decreased the ΔpHD_{50} values significantly, by 22% and 24%, respectively (figure 4*c*). The combination of the seven mutations in the acidic pocket or of the two mutations in the central vestibule that had produced a significant reduction of the ΔpHD_{50}, termed 'AP-SSD' and 'CV-SSD', showed a significant decrease of the ΔpHD_{50} compared with the WT to 0.05 ± 0.11 (n = 8) and 0.13 ± 0.03 (n = 8), respectively (figure 4*d*). These two combined mutants produced transient currents (figure 4*e*) and showed a greater reduction of the ΔpHD_{50} in comparison with the individual mutants (ANOVA and Dunnett's multiple comparisons test; AP-SSD compared with all individual acidic pocket mutants, $p < 0.0001$; CV-SSD compared with E375A and E413A, $p < 0.0001$). Note that these combined mutants are different from AP-Act and CV-Act since the residues mutated in the combined mutants were based on their individual effects on activation in 'Act' and on SSD in 'SSD' mutants. The construct combining the mutations of AP-SSD and CV-SSD was non-functional, which precluded the investigation of the effect of combining all the best candidates.

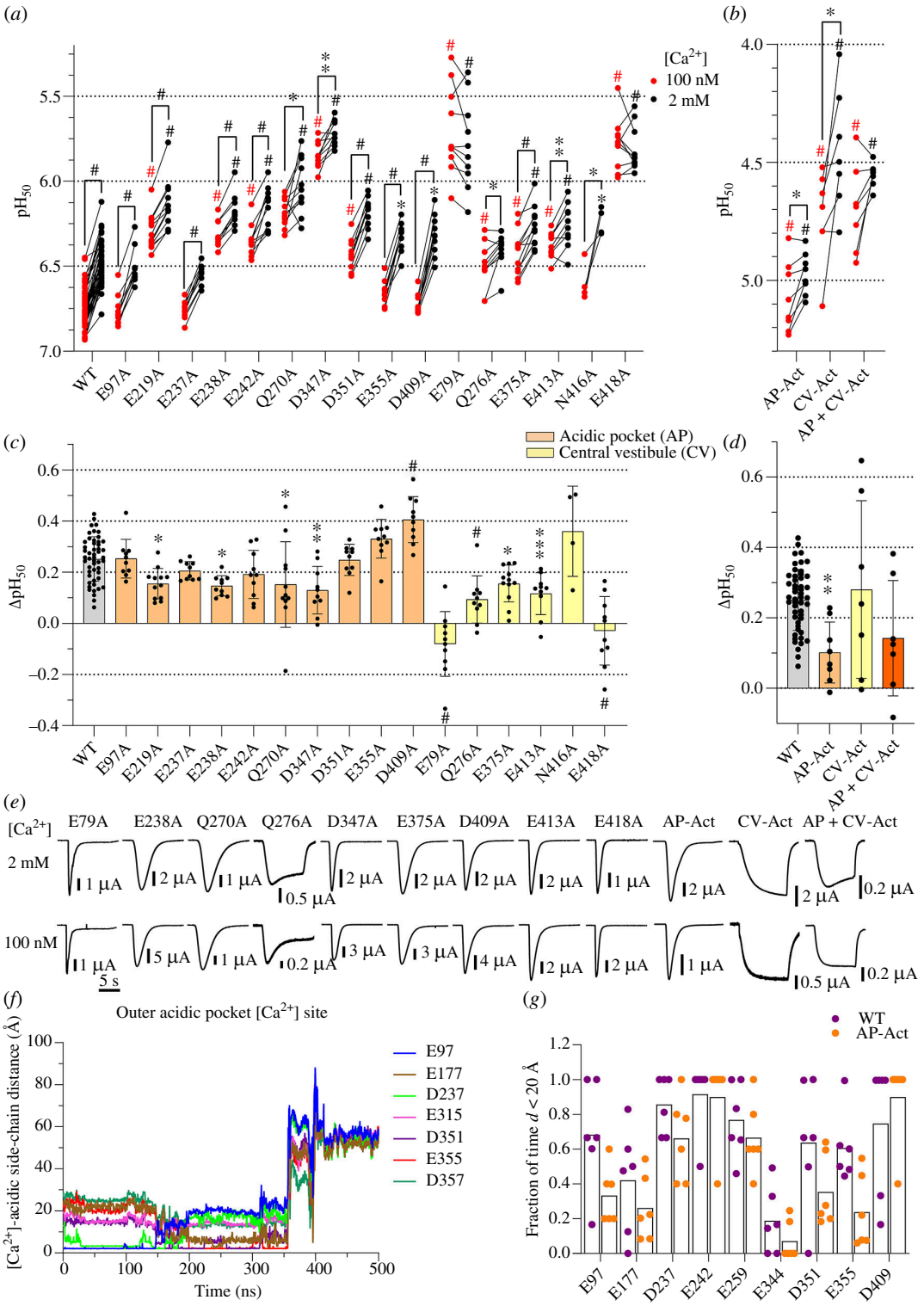

Figure 3. Functional analysis of mutants identifies Ca^{2+}-binding sites for activation in the acidic pocket (AP) and the central vestibule (CV). (*a*,*b*) pH values for half-maximal activation (pH_{50}) were obtained from activation curves with stimulation solutions containing 100 nM free Ca^{2+} (red symbols) or 2 mM Ca^{2+} (black symbols), $n = 4$–53. The pH dependence at 100 nM and 2 mM free Ca^{2+} was measured in the same oocytes. A pH 7.4 was used as the conditioning pH for WT and all mutants except E79A and E418A and CV-Act where a pH 7.8 was used. The mutant AP-Act contains the mutations E219A, E238A, Q270A and D347A. CV-Act contains the mutations E79A, Q276A, E375A, E413A and E418A. The comparison between pH_{50} at 100 nM free Ca^{2+} and 2 mM Ca^{2+} was done by paired *t*-test. For comparisons of pH_{50} values of mutants relative to the WT at 100 nM or 2 mM Ca^{2+}, a one-way ANOVA and Tukey's multiple comparison tests were carried out. $^{*}p < 0.05$; $^{**}p < 0.01$; $^{***}p < 0.001$; $^{\#}p < 0.0001$. (*c*,*d*) ΔpH_{50} ($pH_{50,100\ nM} - pH_{50,2\ mM}$) values are shown as mean ± s.d., $n = 4$–50. Comparison of the mutants to the WT was done by one-way ANOVA and Dunnett's multiple comparison test. $^{*}p < 0.05$; $^{**}p < 0.01$; $^{***}p < 0.001$; $^{\#}p < 0.0001$. (*e*) Representative current traces of mutants showing a significant reduction in the ΔpH_{50} relative to the WT and of the combined mutants. The traces were obtained at the two Ca^{2+} concentrations, at a pH close to the pH_{50}. (*f*) Time course of Ca^{2+}-side-chain distances for one Ca^{2+} ion in the outer AP Ca^{2+} site with distances to finger and thumb residues in the AP-Act mutant, shown for one representative Ca^{2+} ion (out of six) placed in the outer AP Ca^{2+} site. Note that the *y*-axis scale is different from the corresponding figures with WT (figure 2*e*–*g*). (*g*) Fraction of time during which a Ca^{2+} ion was closer than 20 Å to the indicated residue in the AP-Act mutant, measured by MD simulations as for the WT in figure 2*a*.

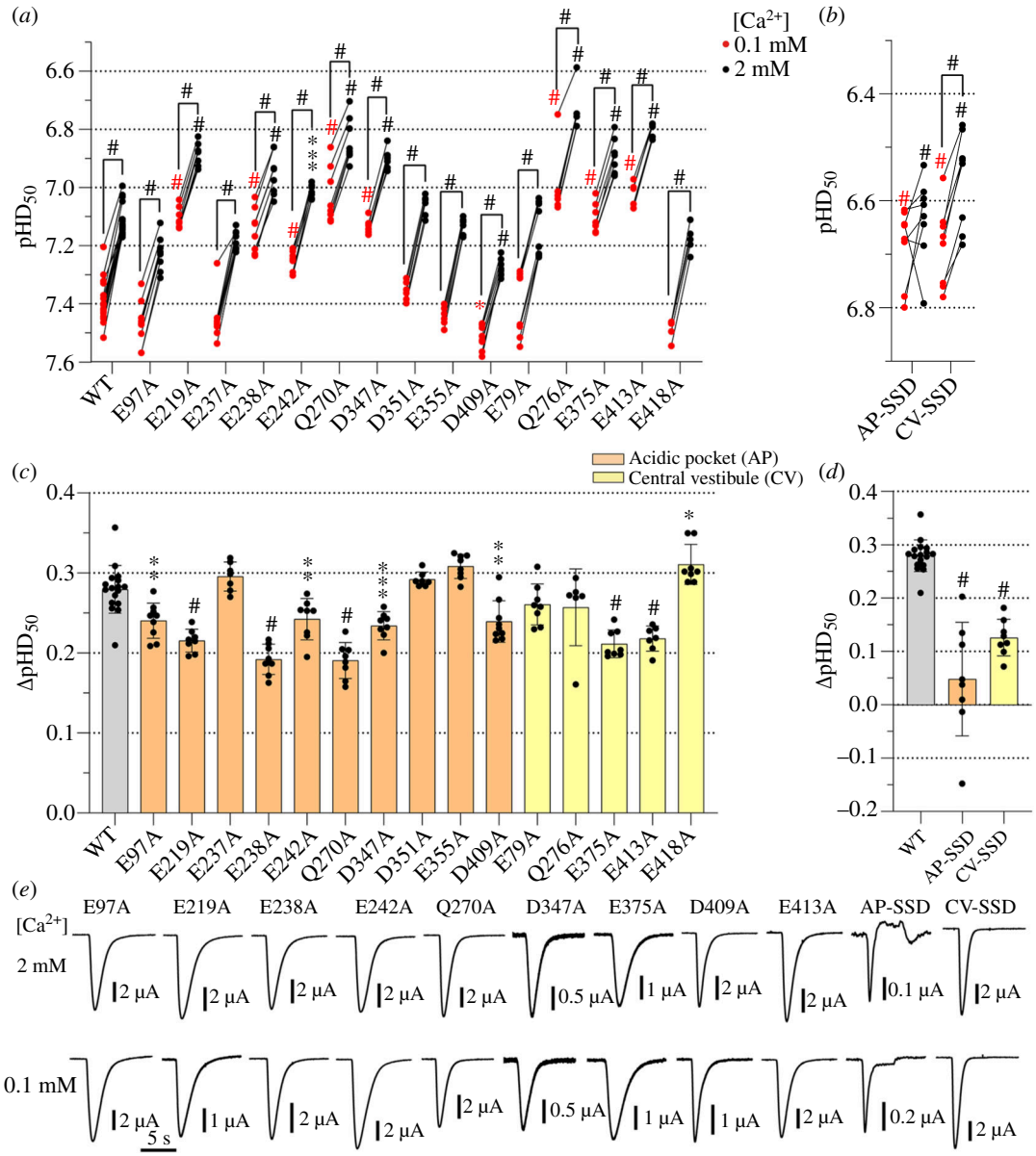

Figure 4. Mutations in the acidic pocket (AP) and the central vestibule (CV) affect the Ca^{2+} modulation of the SSD. (*a,b*) pH values for half-maximal SSD (pHD_{50}) obtained from SSD curves with conditioning solutions containing 0.1 mM Ca^{2+} (red symbols) or 2 mM Ca^{2+} (black symbols), $n = 6–17$. The pH dependence at 0.1 mM and 2 mM Ca^{2+} was measured in the same oocytes. AP-SSD combines the mutations E97A, E219A, E238A, E242A, Q270A, D347A and D409A. CV-SSD combines the mutations E375A and E413A. (*c,d*) ΔpHD_{50} ($pHD_{50,0.1\ mM} – pHD_{50,2\ mM}$) values are shown as mean ± s.d., $n = 6–17$. (*e*) Representative current traces of mutants showing a significant reduction in the ΔpHD_{50} relative to the WT. The traces were obtained at the two Ca^{2+} concentrations, at a pH close to the pHD_{50}. (*a–d*) The same statistical tests as in figure 3 were carried out.

(f) Known Ca^{2+}-binding sites in the pore entry are also involved in the Ca^{2+} modulation of the ASIC1a pH dependence

In addition to modulating the pH dependence, Ca^{2+} has been shown to inhibit ASIC1a by a pore block. Two residues in the pore entry of rat ASIC1a, E425 and D432, were shown to contribute to this effect [17]. We tested whether these two residues were also involved in the modulation of the pH dependence by Ca^{2+}. The corresponding residues in human ASIC1a, E427 and D434 (figure 5*a*) were mutated to Ala. First, the inhibition by Ca^{2+} was measured by exposing WT and mutants to increasing extracellular Ca^{2+} concentrations at pH 5.5, at which the channels are fully activated. In ASIC1a WT, 10 mM Ca^{2+} inhibited 51 ± 9% of the maximal current amplitude (figure 5*b,c*). The inhibition by 10 mM Ca^{2+} amounted to 35 ± 7% with E427A and 16 ± 28% with D434A. For D434A, this reduction was significantly different from the WT ($p < 0.001$), thus similar to the results obtained with the rat ASIC1a mutants [17]. Next, the involvement of these residues in the modulation of the pH dependence by Ca^{2+} was assessed. At 2 mM Ca^{2+}, the pH_{50} and pHD_{50} values of the two mutants were very similar to the corresponding WT values (figure 5*d,e*). The mutation D434A decreased the ΔpH_{50} of activation by half in comparison to the WT (figure 5*d*). The mutation E427A did not affect Ca^{2+} modulation of activation; it reduced, however, the ΔpHD_{50} as compared with WT by 23% (figure 5*e*). This shows that in addition to the Ca^{2+} pore block, the residues E427 and D434 are involved in modulating the pH dependence of human ASIC1a by Ca^{2+}.

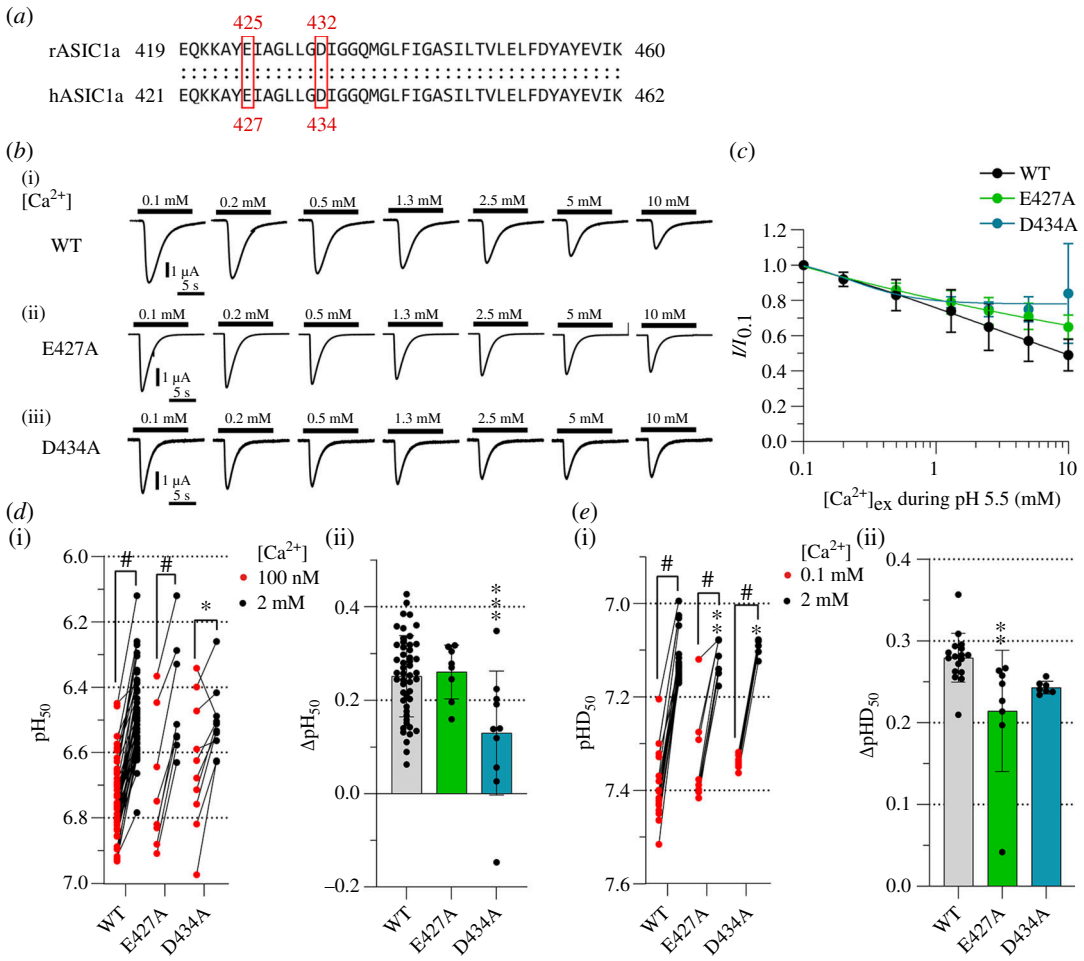

Figure 5. Mutations of two amino acid residues in the pore reduce Ca^{2+} block and modulation of the pH dependence. (*a*) Alignment of amino acid sequences of rat ASIC1a and human ASIC1a at the level of the transmembrane domain TM2. Corresponding conserved acidic residues in the pore entry are highlighted by red frames. (*b*) Representative current traces of ASIC1a WT and mutants obtained by 10 s applications of increasing Ca^{2+} concentrations in pH 5.5 stimulation solutions, as indicated. The Ca^{2+} concentration in the conditioning solution of pH 7.4 was 2 mM. (*c*) Concentration–response curves for Ca^{2+} inhibition of ASIC1a WT and mutants. The lines represent fits to an inhibition equation. (*d*(i)) pH50 and (*e*(i)) pHD_{50} values obtained from activation and SSD curves with stimulation (*d*) or conditioning solutions (*e*) containing low free Ca^{2+} as indicated (red symbols) or 2 mM Ca^{2+} (black symbols), $n = 7–53$. The pH dependence at the two Ca^{2+} concentrations was measured in the same oocytes. A paired *t*-test was used to compare the pH_{50} or pHD_{50} values between the two Ca^{2+} conditions, and a one-way ANOVA with Tukey's multiple comparison test to compare the pH_{50} or pHD_{50} values of mutants to the WT in the corresponding Ca^{2+} condition. ΔpH_{50} ($pH_{50,100\ nM} – pH_{50,2\ mM}$ (*d*(ii)) or ΔpHD_{50} ($pHD_{50,0.1\ mM} – pHD_{50,2\ mM}$ (*e*(ii)); data are shown as mean ± s.d. Comparison of the mutants to the WT was done by one-way ANOVA and Dunnett's multiple comparison test. $^{*}p < 0.05$; $^{**}p < 0.01$; $^{***}p < 0.001$; $^{\#}p < 0.0001$.

(g) Stabilization of the ASIC1a resting state by Ca^{2+} demonstrated by mutations of two central vestibule residues

Increasing the extracellular Ca^{2+} concentration from 0.1 mM to 2 mM shifted the pH dependence of SSD to more acidic values for ASIC1a (figure 1*d*), thereby increasing the number of available channels at a given pH. It is expected that an increase in Ca^{2+} concentration will, at a given pH, increase the rate of recovery and/or slow the rate of desensitization from the closed state [15]. The central vestibule is enclosed by the lower palm domain of the three subunits, which is involved in desensitization from open and closed states [31]. We have shown that the residue E375 and E413, located in the central vestibule, are involved in Ca^{2+} coordination modulating SSD (figure 4*c*). To further investigate their roles in the stabilization of the ASIC1a resting state by Ca^{2+}, the rate of recovery from desensitization after exposure to pH 6.0 was measured by exposing the desensitized channels during increasing periods to conditioning pH 7.4 with a Ca^{2+}concentration of 2 mM or 0.1 mM, before a second stimulation by pH 6.0 (figure 6*a*). For WT ASIC1a, a slower time constant of recovery from desensitization was observed at 0.1 mM Ca^{2+} (22.8 ± 15.3 s, $n = 10$) compared with 2 mM Ca^{2+} (4.0 ± 3.1 s, $n = 10$; figure 6*b*). As a measure of the modulatory effect of Ca^{2+}, the $\tau_{0.1\ mM\ Ca}/\tau_{2\ mM\ Ca}$ ratio was calculated in each experiment, which was 8.3 ± 6.2 for the WT (figure 6*c*; $n = 10$). The pH during the recovery period of ASIC1a WT was 7.4 with both Ca^{2+} conditions, which is 0.26 pH units above its pHD_{50} in the presence of 2 mM Ca^{2+} (figure 1*d* and 4*a*). Since the pH dependence of SSD of the two mutants was shifted to more acidic values, the pH in the conditioning solutions was adapted for the mutants to pH 7.1 for E375A and pH 7.0 for E413A. At 2 mM Ca^{2+}, E413A showed a time constant of recovery that was very close to that of the WT, while the recovery kinetics of E375A were 8.9 ± 6.6 s ($n = 7$) and therefore somewhat slower. The effect of the Ca^{2+} concentration change was significantly smaller in the mutants, with a $\tau_{0.1\ mM\ Ca}/\tau_{2\ mM\ Ca}$ ratio of 1.5 ± 0.6 ($n = 7$) for E375A and 1.8 ± 0.7 ($n = 8$) for E413A (figure 6*c*), as further illustrated by smaller shifts in the recovery curves (figure 6*b*).

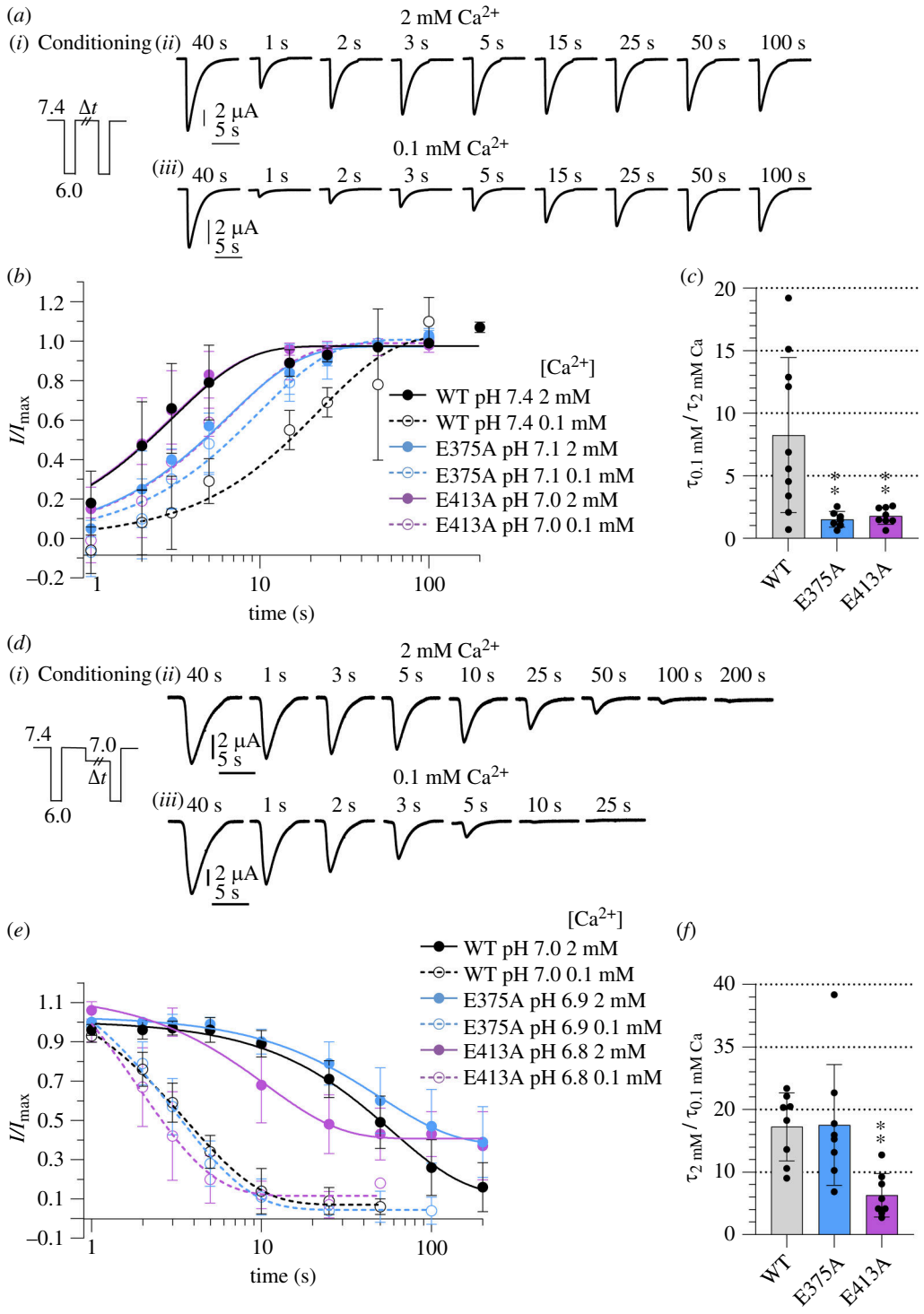

Figure 6. Mutations affecting Ca^{2+} modulation change the kinetics of transitions in and out of the desensitized state. (*a*) Representative current traces of ASIC1a WT recovery from desensitization experiments, following the protocol illustrated in (i). Two stimulations to pH 6.0 were separated by an interval of increasing duration at the conditioning solution of pH 7.4 containing 2 mM Ca^{2+} (ii) or 0.1 mM Ca^{2+} (iii). The duration of the conditioning interval at pH 7.4 is indicated above each trace. (*b*) Current peak amplitudes normalized to the control current amplitude of each recovery protocol are plotted as a function of the duration at the conditioning solution between the two paired stimulations to pH 6.0, $n = 7–10$. The connecting lines are fits to a single exponential. The conditioning pH used for the different constructs is indicated in the figure. (*c*) τ ratios ($\tau_{0.1\ mM\ Ca}/\tau_{2\ mM\ Ca}$) calculated from the fits to the recovery time course, $n = 7–10$. Comparison between the mutants and the WT was done by one-way ANOVA and Dunnett's multiple comparison test. $^{*}p < 0.05$; $^{**}p < 0.01$; $^{***}p < 0.001$; $^{\#}p < 0.0001$. (*d*) Representative ASIC1a current traces from the onset of SSD protocol, as illustrated in (i). A 3.5 s pH 6.0 stimulation (control response) was applied before the application of pH 7.4 for 50 s to allow the channel to recover completely from desensitization. Subsequently, the WT channels were exposed to a conditioning pH 7.0 whose duration was increased in each round, followed by a second stimulation with pH of 6.0. The test conditioning solution contained 2 mM (ii) or 0.1 mM Ca^{2+} (iii). The duration of the conditioning period is indicated above each trace. (*e*) Current peak amplitudes normalized to the control current amplitude of each desensitization onset protocol, plotted as a function of the conditioning period, $n = 8$. The conditioning pH used for the different constructs is indicated in the figure. The connecting lines represent exponential fits. (*f*) τ ratios ($\tau_{2\ mM\ Ca}/\tau_{0.1\ mM\ Ca}$) obtained from the fit of the normalized current peak amplitudes of the onset of SSD protocol, $n = 8$. Comparison of the mutants to the WT was done by one-way ANOVA and Dunnett's multiple comparison test. $^{*}p < 0.05$; $^{**}p < 0.01$; $^{***}p < 0.001$; $^{\#}p < 0.0001$.

To study the inverse transition, the onset of SSD, channels were exposed during varying periods to a pH that induces desensitization, pH 7.0 for WT, pH 6.9 for E375A and pH 6.8 for E413A (figure 6*d*). These pH values were chosen because they desensitize the channels by approximately 50% after a 50 s exposure to the conditioning pH at 2 mM Ca^{2+}. The fraction of channels having not yet entered the desensitized state was determined as the ratio of the pH 6.0-induced current measured after exposure to the desensitizing pH/control current amplitude (figure 6*e*). In WT ASIC1a, the onset of SSD at 0.1 mM Ca^{2+} ($\tau_{0.1\ mM\ Ca}$ = 3.9 ± 1.3 s, n = 8) was faster than in the presence of 2 mM Ca^{2+} ($\tau_{2\ mM\ Ca}$ = 63.6 ± 22.7; figure 6*e,f*) with a $\tau_{2\ mM\ Ca}/\tau_{0.1\ mM\ Ca}$ ratio of 17.3 ± 5.4 (n = 8). This is expected since lowering the Ca^{2+} concentration shifts the pHD_{50} to more alkaline values. Ca^{2+} induced a similar shift in WT and also in E375A, while in E413A, the $\tau_{2\ mM\ Ca}/\tau_{0.1\ mM\ Ca}$ ratio was 6.3 ± 3.5 (n = 8), significantly lower than the WT value. In conclusion, both mutations impaired the Ca^{2+} modulation of the recovery from desensitization, while only E413A affected the onset of SSD.

(h) Mg^{2+} shares binding sites for steady-state desensitization modulation with Ca^{2+}

In a previous study, in which Ca^{2+} and Mg^{2+} concentrations were changed together, Mg^{2+} appeared to modulate the ASIC1a pH dependence similarly to Ca^{2+} [15]. In our experimental conditions, in the absence of extracellular Ca^{2+}, the pH_{50} of activation was 6.59 ± 0.11 (n = 14) at 2 mM Mg^{2+} and 6.72 ± 0.11 (n = 14) at 100 nM Mg^{2+}, indicating an alkaline ΔpH_{50} of 0.13 ± 0.07 pH units with the lower Mg^{2+} concentration (figure 7*a*). For the SSD, decreasing the Mg^{2+} concentration from 2 mM to 0.1 mM did not significantly change the pHD_{50}. Therefore, the two conditions 10 mM and 0.1 mM Mg^{2+} were compared. A pHD_{50} of 6.97 ± 0.07 (n = 8) was obtained with 10 mM Mg^{2+}, while the pHD_{50} at 0.1 mM Mg^{2+} was 7.37 ± 0.09 (n = 8), indicating a shift towards more alkaline pH_{50} values by 0.39 ± 0.03 pH units with the lower Mg^{2+} concentration.

To determine whether Ca^{2+} and Mg^{2+} ions may share binding sites for modulation of the activation pH dependence, the ΔpH_{50} induced by a change in Mg^{2+} concentration was measured with the previously established combined mutants for Ca^{2+} modulation (figure 3). At 2 mM Mg^{2+}, the pH_{50} of the two combined mutants was strongly shifted towards acidic values in comparison to the WT (figure 7*b*(i)), as observed previously in the 2 mM Ca^{2+} conditions (figure 3*b*). The ΔpH_{50} between the two Mg^{2+} concentrations obtained with the mutants was not significantly different from the WT value (figure 7*b*(ii)), as opposed to the effects of changing the Ca^{2+} concentration on the AP-Act mutant (figure 3*d*). The absence of an effect with the AP-Act mutant may be owing to the fact that in the WT, the Mg^{2+}-induced pH_{50} shift was very small, or because of the differential binding of Ca^{2+} and Mg^{2+}. An analogous analysis was carried out for the SSD with the previously described combined mutants AP-SSD and CV-SSD (figure 4). The pHD_{50} values of the mutants at 10 mM Mg^{2+} were also shifted to more acidic values relative to WT (figure 7*c*), as observed with 2 mM Ca^{2+} (figure 4*b*). In both mutants, the Mg^{2+}-dependent shift was strongly and significantly reduced to 0.07 ± 0.02 (n = 8, AP-SSD) and 0.15 ± 0.06 (n = 8, CV-SSD; figure 7*c*). This indicates that Mg^{2+} modulates desensitization and shares binding sites with Ca^{2+} for desensitization.

(i) Conservation of Ca^{2+}binding sites in ASIC1b

ASIC1b is expressed in the peripheral but not the central nervous system and has a lower apparent affinity for H^+ compared with ASIC1a [15,32]. ASIC1a and ASIC1b are splice variants differing in the N-terminal by approximately 180 residues, which correspond to the first transmembrane segment, the finger and parts of the palm and β-ball domains. Thus, the acidic pocket and pore-lining parts are mostly conserved between ASIC1a and ASIC1b, while parts of the central vestibule are different. The alignment between ASIC1a and ASIC1b (electronic supplementary material, figure S3) indicates that all ASIC1a residues involved in Ca^{2+} regulation, except for Glu97, are conserved in ASIC1b. Ca^{2+} was shown to shift the SSD curve of ASIC1b similarly to ASIC1a and the activation curves to a lesser extent [15]. Our measurements confirmed the previous data on ASIC1b, with pH_{50} values of 6.13 ± 0.06 (n = 9) at 2 mM Ca^{2+} and 6.33 ± 0.07 (n = 9) at 100 nM Ca^{2+} (figure 8*a*) and pHD_{50} values of 7.13 ± 0.07 (n = 9) at 2 mM Ca^{2+} and 7.37 ± 0.04 (n = 9) at 0.1 mM Ca^{2+}. The ΔpH_{50} and ΔpHD_{50} induced by changes in extracellular Ca^{2+} concentration are therefore similar between ASIC1a and ASIC1b. To determine whether the Ca^{2+}-binding sites are functionally conserved in ASIC1, the homologous combined mutations to AP-Act, CV-Act, AP-SSD and CV-SSD, previously constructed in ASIC1a, were generated in ASIC1b, with the difference that the non-conserved ASIC1a-E97A mutation could not be included in ASIC1b. The ASIC1b AP-Act and CV-Act mutants appeared to have a strong acidic shift of their pH dependence with current amplitudes still increasing at pH 3, and a high variability, precluding therefore a precise measurement of the activation pH dependence. For the SSD, the WT ΔpHD_{50} was 0.24 ± 0.06 (n = 9; figure 8*b*). The ΔpHD_{50} of the mutant AP-SSD was not significantly different from the WT value (0.17 ± 0.27 (n = 12)), while in CV-SSD, the regulation of the SSD pH dependence by Ca^{2+} was suppressed, with a pHD_{50} value of –0.14 ± 0.30 (n = 10; figure 8*b*). These two combined mutants produced transient currents with a sustained current component (figure 8*c*). To conclude, the Ca^{2+}-binding site for desensitization of the central vestibule is conserved between ASIC1a and ASIC1b. Owing to the strong changes in the basic properties of the combined mutants for activation, our analysis does not provide an ultimate answer to the functional conservation of the Ca^{2+}-binding sites for activation between the two splice variants.

3. Discussion

Extracellular Ca^{2+} competes with protons for binding sites on ASIC1a and modulates its pH dependence. Based on published crystal structures obtained in the presence of divalent cations and our MD simulations with a structural ASIC1a model, specific

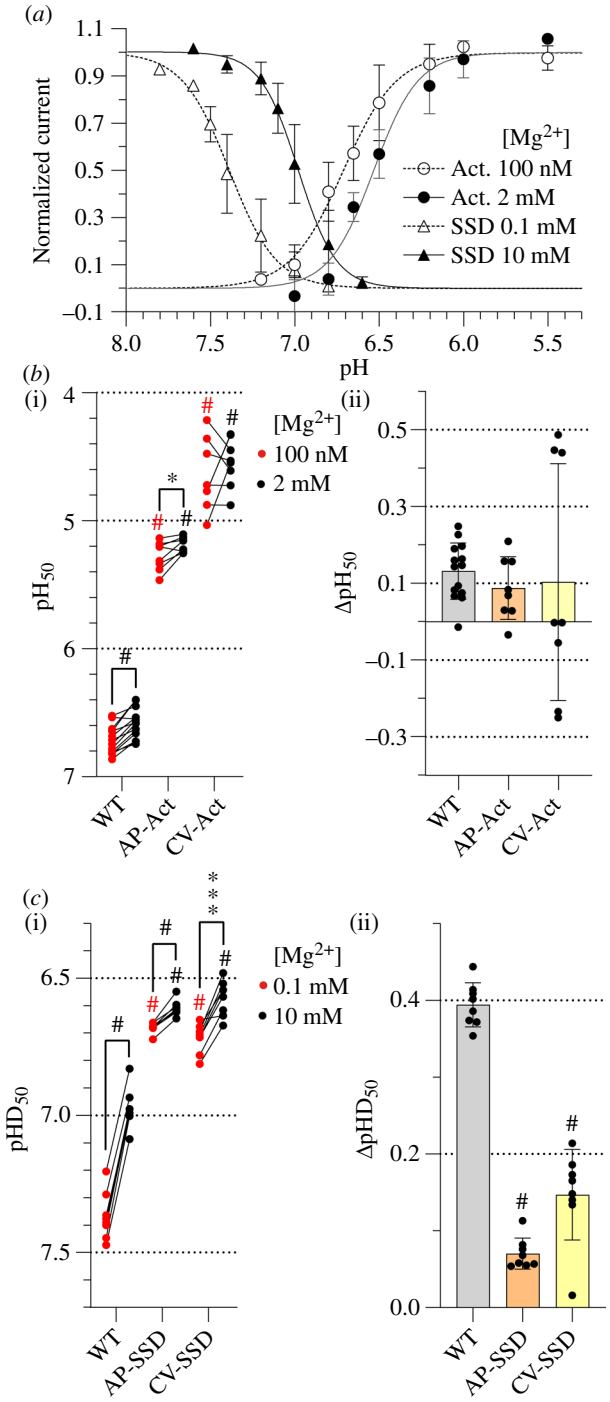

Figure 7. Magnesium modulates ASIC1a activation and desensitization of ASIC1a and shares binding sites with Ca^{2+} for desensitization. (*a*) pH dependence curves of activation and SSD of ASIC1a ($n = 8–14$). Activation curves were measured at 100 nM free Mg^{2+} (open circles) or 2 mM Mg^{2+} (filled circles) in the stimulation solution in the absence of Ca^{2+}. SSD curves were measured at 0.1 mM Mg^{2+} (open triangles) or 10 mM Mg^{2+} (filled triangles) in the conditioning solution, in the absence of Ca^{2+}. The pH of the conditioning solution of activation experiments was 7.4 and that of the stimulation solution of SSD experiments was 5.0; both solutions contained 2 mM Mg^{2+}. Currents are normalized to the maximum peak current. The lines represent fits to the Hill equation. A representative data set is shown. (*b*,*c*) pH_{50} (*b*(i)) and pHD_{50} values (*c*(i)) obtained from activation and SSD curves with stimulation (*b*) or conditioning solutions (*c*) containing low free Mg^{2+} (red symbols) or high free Mg^{2+} (black symbols) as indicated, $n = 8–14$. The pH dependence at low and high free Mg^{2+} was measured in the same oocytes. The comparison of the two Mg^{2+} conditions was analysed with a paired *t*-test, and the difference to WT values was analysed with one-way ANOVA followed by Tukey's multiple comparison test. ΔpH_{50} ($pH_{50,100\ nM} - pH_{50,2mM}$) (*b*(ii)) or ΔpHD_{50} ($pHD_{50,0.1\ mM} - pHD_{50,10\ mM}$(*c*(ii)) are shown as mean ± s.d., $n = 8–14$. Comparison of the mutants to the WT was done by one-way ANOVA and Dunnett's multiple comparison test. $^{*}p < 0.05$; $^{**}p < 0.01$; $^{***}p < 0.001$; $^{\#}p < 0.0001$.

residues of the acidic pocket and the central vestibule were predicted to interact with Ca^{2+} ions. Mutation of candidate residues and functional analysis showed that E219, E238, Q270 and D347 of the acidic pocket, E79, Q276, E375, E413 and E418 of the central vestibule and D434 of the pore entry contribute to the Ca^{2+} modulation of activation, while E97, E219, E238, E242, Q270, D347 and D409 of the acidic pocket, E375 and E413 of the central vestibule and E427 of the pore entry contribute to its modulation of the SSD (figure 9*a*,*b*). We show that of the two Ca^{2+}-binding sites in each acidic pocket, the outer site, comprising residues E238 and D347, is more important for activation than the inner site. We show here also that Mg^{2+} ions share binding

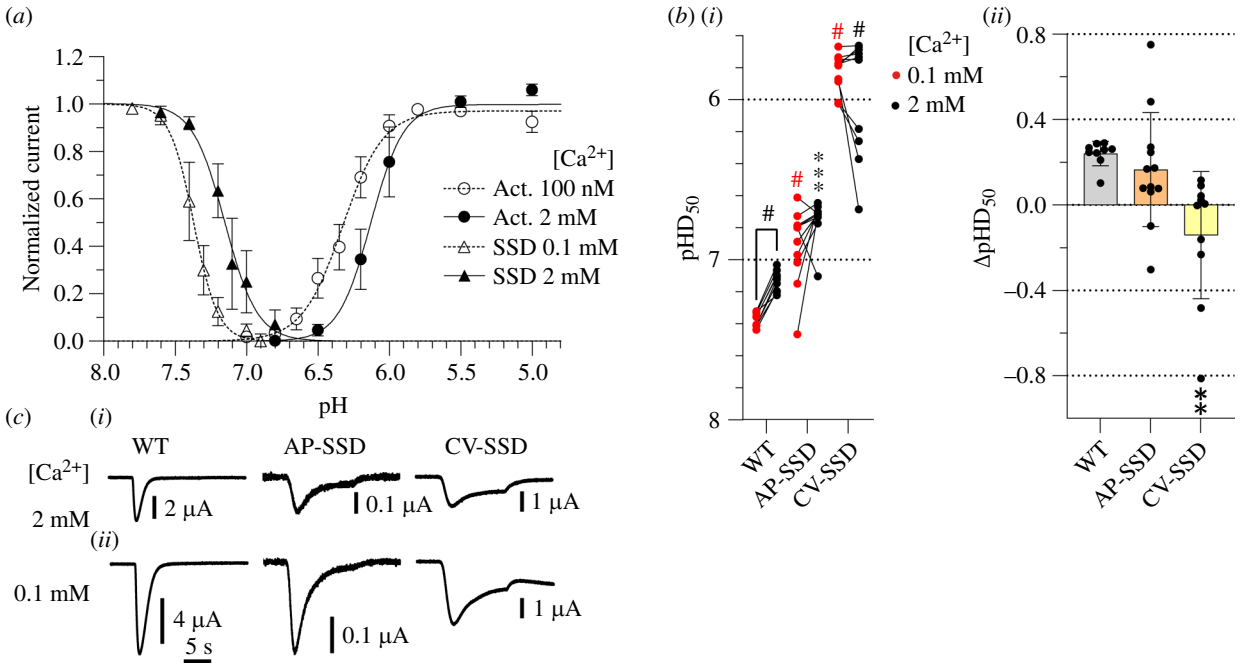

Figure 8. ASIC1b shares Ca^{2+}-binding sites for SSD with ASIC1a in the central vestibule. (*a*) pH dependence curves of activation and SSD of ASIC1b ($n = 9$). Activation curves were measured at 100 nM free Ca^{2+} (open circles) or 2 mM Ca^{2+} (filled circles) in the stimulation solution. SSD curves were measured at 0.1 mM Ca^{2+} (open triangles) or 2 mM Ca^{2+} (filled triangles) in the conditioning solution. The conditioning solution of activation experiments and the stimulation solution of SSD experiments contained 2 mM Ca^{2+}. Currents were normalized to the maximum peak current. The lines represent fits to the Hill equation. (*b*(i)) pHD_{50} values obtained from SSD curves with conditioning solutions containing 0.1 mM Ca^{2+} (red symbols) or 2 mM Ca^{2+} (black symbols) as indicated, $n = 9–12$. The comparison of the two Ca^{2+} conditions was analysed with a paired *t*-test, and the difference between mutant and WT pHD_{50} values was analysed with one-way ANOVA followed by Tukey's multiple comparison test. (*b*(ii)) ΔpHD_{50} ($pHD_{50,0.1\ mM} - pHD_{50,2\ mM}$) values, shown as mean ± s.d., $n = 9–12$. Comparison of the mutants to the WT was done by one-way ANOVA and Dunnett's multiple comparison test. *$p < 0.05$; **$p < 0.01$; ***$p < 0.001$; #$p<0.0001$. The pH dependence at 0.1 mM and 2 mM Ca^{2+} was measured in the same oocytes. AP-SSD combines the mutations E206A, E225A, Q257A, E229A, D332A and D394A. CV-SSD combines the mutations E360A and E398A. (*c*) Representative current traces of WT and combined mutants. The traces were obtained at the two Ca^{2+} concentrations, at a pH close to the pHD_{50}.

sites with Ca^{2+} for desensitization in both the acidic pocket and the central vestibule. In addition, the Ca^{2+}-binding sites for desensitization in the central vestibule are functionally conserved between the splice variants ASIC1a and ASIC1b.

In the mammalian brain, basal interstitial Ca^{2+} and Mg^{2+} concentrations are between 1 and 2 mM. Strong neuronal activity, a seizure or an ischaemic stroke can lower the extracellular Ca^{2+} concentration down to 0.1 mM [7–9]. During ischaemia, the anaerobic metabolism produces lactate, which chelates Ca^{2+} [33]. Mg^{2+} is one of the most abundant ions and is a cofactor of many enzymes in neurons and glia. Low levels of Mg^{2+} have been associated with pathological conditions such as ischaemic stroke, Alzheimer's disease or migraine headaches [34]. Also, Mg^{2+} depletion has been reported after brain injury, while Mg^{2+} administration has shown neuroprotective effects [35].

Calcium interacts in binding sites primarily with charged amino acid side chains but also with main-chain carbonyl oxygen atoms [36]. With the mutagenesis approach that does not change the peptide backbone, our study does not address the role of main-chain carbonyls in the ASIC1a Ca^{2+}-binding sites. The potential involvement of backbone carbonyls could be investigated by using unnatural amino acids with different backbone structures [37].

Calcium and Mg^{2+} bind to proteins either in the dehydrated or hydrated state. Although the interaction of dehydrated Ca^{2+} and Mg^{2+} ions with proteins differ [10], those of the hydrated ions are quite similar. Magnesium interacts in binding sites generally with less atoms and at smaller distances than Ca^{2+} [38]. In troponin C, for example, Ca^{2+} has been shown to coordinate an additional glutamate compared with Mg^{2+}, which may be critical for the selectivity between these two ions and may explain the higher affinity for Ca^{2+} [39]. The Ca^{2+}-permeable *N*-methyl-D-aspartic acid glutamate channels are inhibited by physiological Mg^{2+} concentrations by open channel block [40], also showing different functions of these two ions. The modulation of ASIC1a by Ca^{2+} and Mg^{2+} is qualitatively similar. We show, however, for ASIC1a that Mg^{2+} shifts the pH dependence less than Ca^{2+} and that Mg^{2+} appears to share binding sites with Ca^{2+} only for desensitization.

Lowering the extracellular Ca^{2+} concentration increases the activity of voltage-gated Na^+ channels [10], the Na^+ leak channel (NALCN) [11] and the Ca^{2+} homeostasis modulator 1 (CALHM1) [12]. For voltage-gated Na^+ channels, it was concluded that the effects of Ca^{2+} were owing to surface charge screening. The inhibition of NALCN is likely owing to pore block [11], while Ca^{2+} was shown to interact with an Asp residue of CALHM1 located outside the permeation pathway [12].

In ASIC3, lowering of the extracellular Ca^{2+} concentration induces a considerably stronger shift of the activation pH dependence than in ASIC1a [18], and removal of the extracellular Ca^{2+} at physiological pH 7.4 activates ASIC3 [16] but not ASIC1a. Consistent with a smaller modulatory contribution of Ca^{2+} to ASIC1a as compared with ASIC3 gating, the apparent affinity of Ca^{2+} for the shift in activation pH dependence was 3.5 mM in ASIC1a (figure 1*e*,*f*), compared with 41 µM in ASIC3 [18]. An ASIC3 gating model was proposed in which acidification opens ASIC3 by inducing unbinding of Ca^{2+} ions from the pore entry [16]. Consistent with this hypothesis, ASIC3–Glu435, a pore residue not conserved in ASIC1a (the residue at the

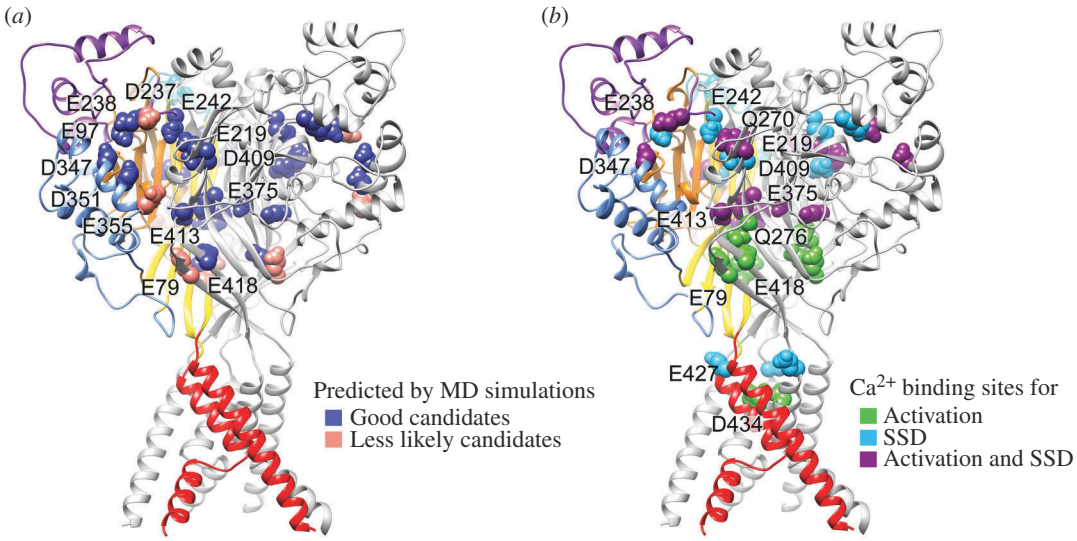

Figure 9. Predicted and confirmed residues for Ca^{2+}-binding sites in ASIC1a. Structural images of an ASIC1a trimer in the closed state, from a model based on the crystal structure (5WKU). The different domains are indicated by specific colours in one of the three ASIC subunits, while the two others are represented in grey. (*a*) Residues predicted by MD simulations as Ca^{2+}-binding sites are indicated by two different colours to distinguish the good candidates from the less likely candidates. (*b*) Residues identified by functional analysis as Ca^{2+}-binding sites are coloured depending on their involvement in activation, SSD or both.

homologous position in hASIC1a is Gly430), was identified as important for the ASIC3 modulation by Ca^{2+} [19]. Recently, we identified additional residues that contribute to a similar extent as Glu435 to Ca^{2+} modulation of ASIC3 activation, Asp439 (corresponding to Asp434 in hASIC1a) in the pore entry and Glu212 (corresponding to Glu219 in hASIC1a) of the acidic pocket, showing, to our knowledge, for the first time a contribution of residues outside the pore entry to ASIC3 modulation by Ca^{2+} [18]. Three residues were involved in the Ca^{2+} regulation of ASIC3 SSD, Glu212 and Glu235 of the acidic pocket (corresponding to Glu219 and Glu242 in hASIC1a) and Asn421 of the lower palm (corresponding to Asn416 in hASIC1a) [18]. Functional observations indicate that ASIC1a is activated by H^+-induced allosteric changes [41]. Further support for an allosteric activation mechanism comes from voltage-clamp fluorometry experiments providing evidence for conformational changes linked to ASIC1a activation [27–30] and from the observation that mutation of the two residues involved in ASIC1a pore block by Ca^{2+} did not abolish pH-dependent gating [17]. The E425G mutation decreased the Ca^{2+}-induced shift of the pH dependence of SSD, while D432C decreased the Ca^{2+}-induced shift of the activation pH dependence [17]. The statistical significance of this difference relative to WT was, however, not analysed. By mutating the corresponding residues in human ASIC1a, E427 and D434, to Ala, we confirmed these earlier findings, showing that these two residues in the pore are involved in the modulation effect of Ca^{2+}.

Compared with ASIC3 in which binding sites in the pore and the acidic pocket contribute to Ca^{2+} modulation of activation, ASIC1a has additional binding sites in the central vestibule involved in activation (figure 9*b*). Regarding SSD modulation, the acidic pocket and central vestibule are involved in both ASIC1a and ASIC3, with an additional small contribution of the pore residue Glu427 in ASIC1a (figure 9*b*). In ASIC1a, 10 out of 17 tested mutations decreased the Ca^{2+} modulation of SSD, with individual mutations having however small effects (figure 4*c*).

The comparable effect of Ca^{2+} on ASIC1a and ASIC1b in a previous study [15] suggested conserved binding sites. However, our functional analysis of ASIC1b confirmed only the conservation of Ca^{2+}-binding sites in the central vestibule for desensitization. The pH dependence of the combined mutants for activation was too strongly shifted for reliable measurement, and the SSD Ca^{2+} modulation of the combined acidic pocket mutant for desensitization was not significantly different from WT. Functional analyses of individual mutations in ASIC1b would probably provide additional information on the conservation of the Ca^{2+} binding sites for activation.

X-ray crystallography analysis showed that in the high-pH resting state of chicken ASIC1a, two Ba^{2+} ions bind to each acidic pocket and three to the central vestibule [20]. In the desensitized state, only one Ba^{2+} site per acidic pocket remained, and no Ba^{2+} sites were found in the central vestibule. It also needs to be considered that ASIC1a opening and desensitization require an acidic pH, which probably leads to protonation and therefore neutralization of the negative charge of some acidic residues in the proximity of Ca^{2+}-binding sites, disfavouring cation binding. The Ba^{2+} binding was not determined on the open ASIC1a structure. Since the conformation of the acidic pocket is similar in the open and desensitized state, it is reasonable to assume that each acidic pocket of an open ASIC1a can also accommodate one Ca^{2+} ion. Our MD simulations were carried out with a model of the closed conformation of ASIC1a, with a protonation status mimicking pH 7.4. In this conformation, one of the two Ca^{2+} ions of each acidic pocket remained close to E219 and D409, the position that we named 'inner AP Ca^{2+} site' (figures 2*c* and 9*a*). The Ca^{2+} ion initially placed in the outer AP Ca^{2+} site had more dynamic interactions, changing its proximity from E97 to mostly D347 and D351, precluding a precise localization of the second Ca^{2+}-binding site in the acidic pocket. The single Ba^{2+} remaining in each acidic pocket in the desensitized conformation is located between residues corresponding to D237 and E219 of hASIC1a [20], thus overlapping with the inner AP Ca^{2+} site (figure 2*c*). The outer AP Ca^{2+} site is therefore only occupied in the resting state, conferring stabilization of the resting state by Ca^{2+}. In MD simulations with the AP-Act mutant (figure 3*d*), five of six Ca^{2+} ions placed in the outer AP site left the acidic pocket before the end of the 500 ns simulation (figure 3*f*), unlike the

WT construct where none of the six outer AP site Ca^{2+} ions left the acidic pocket during the 600 ns simulation. This indicates a stabilization of the Ca^{2+} ion in the acidic pocket by residues E238 and D347.

In the central vestibule, E375 and E413 are located higher up than E79 and E418 (figure 2*d*). In many MD trajectories, the Ca^{2+} ions of the central vestibule were closer to E375 and E413 than to E79 and E418. The central vestibule gets narrower during both the closed–open and the open–desensitized transitions [42,43]. Therefore, although no Ba^{2+} binding in the central vestibule was observed in the desensitized structure, it cannot be excluded that the open ASIC1a could accommodate divalent cations in the central vestibule.

E427 and D434 contribute to the Ca^{2+}-binding site in the pore. The conformation of the pore strongly changes upon channel opening. In the closed conformation, the distances between side-chain oxygen atoms of different subunits are approximately 4 Å for D434 and approximately 16 Å for E427, and the distance between the side-chain oxygen of D434 and E427 of the same subunit is approximately 12 Å. In the open conformation, these intersubunit distances are approximately 13 Å for D434 and approximately 24 Å for E427. The D434 intersubunit distance of the side-chain oxygens in the closed state of approximately 4 Å is compatible with Ca^{2+} binding [44,45]. Interestingly, however, no divalent binding to the pore was observed in the study by Yoder & Gouaux [20] nor by our MD simulation analysis.

The structure and MD simulations had correctly predicted several residues in the acidic pocket and central vestibule contributing to modulation of Ca^{2+} modulation of activation and SSD. The functional analysis showed in addition that the outer AP Ca^{2+} site was more involved in activation (E238 and D347), while residues of both acidic pocket sites contributed to Ca^{2+} modulation of SSD (figure 9*b*). Regarding the residues of the central vestibule, mutation of all four residues impaired Ca^{2+} modulation of activation, with the E79 and in part the E418 mutation exhibiting more pronounced effects compared with mutation of the other two residues. In contrast, only E375 and E413 contributed to the Ca^{2+} modulation of SSD. Some residues that appeared to contribute to Ca^{2+} binding sites based on the structural information or MD simulations turned out not to participate in the functional regulation, as D351 and D409 for activation. Despite the close distance of residue D409 from divalent cations in X-ray crystallography analyses and MD simulations, its mutation to Ala even favoured Ca^{2+} modulation of activation, as evidenced by the increased shift in the pH dependence of activation. In contrast, the D409A mutation decreased the Ca^{2+}-induced shift in the SSD pH dependence. A difference between the structure analyses and the functional studies is the fact that Ba^{2+} was used in the structure determination, which has a larger ionic radius than Ca^{2+}. The MD simulations were done with the closed conformation of ASIC1a and did therefore not take into account the transitions from the closed to the open or desensitized state, which obviously affected the functional effects of Ca^{2+}, as shown by the different effects of mutations on the modulation of activation versus SSD.

The protonation sites governing ASIC1a activation and desensitization are probably located in the acidic pocket, the central vestibule and the wrist/pore entry [21–25,27]. While H^+ binding promotes the activation and desensitization transitions, Ca^{2+} ions stabilize the closed state, competing thereby with H^+. Ca^{2+} appears not to affect the transitions or the equilibrium between the open and desensitized states, since there were no obvious differences in desensitization kinetics or sustained current amplitudes between the two tested Ca^{2+} concentrations (traces in figure 3*e*). Mutation of several amino acid residues identified as Ca^{2+}-binding sites reduced the H^+-sensitivity at physiological Ca^{2+} concentrations, suggesting that they may be involved in H^+-sensing in ASIC1a. Some combined mutants strongly shifted the H^+-sensitivity and/or disrupted desensitization. Since the properties of these combined mutants were completely different from those of the WT, they could not be used for a reliable analysis of the effect of the combination of these particular mutations on Ca^{2+} modulation of a normal, transient ASIC current. As an alternative to the combination of large numbers of mutations leading to changes in basic channel properties, it will be interesting to test whether combining 2–3 mutations would be sufficient to suppress the Ca^{2+} binding while keeping WT-like basic functional properties.

In conclusion, a change of Ca^{2+} or Mg^{2+} concentrations occurs in certain physiological or pathological conditions, affecting ASIC activity and thus neuronal signalling. We show here that residues in the acidic pocket, the central vestibule and the pore entry contribute to Ca^{2+} modulation of the ASIC1a pH dependence, which is probably owing to the competition of Ca^{2+} for protonation sites controlling activation and desensitization.

4. Material and methods

(a) Molecular dynamics simulations

The homology models for the MD simulations were constructed based on the cryo-EM structure with the accession code 6VTE [46,47], with the termini acetylated and methylated, using in-house CHARMM and Python scripts. The all-atom MD simulations were performed with the CHARMM36 force field, using the GROMACS package v. 2020.4. The models were inserted in 1-palmitoyl-2-oleoyl-sn-glycero-3-phosphocholine bilayers comprising 592 lipids and hydrated (model TIP3 [48]) at 150 mM NaCl. The initial positions of the Ca^{2+} ions were set to correspond to the positions published in the study by Yoder & Gouaux [20]. Two such systems were combined in an antiparallel way to form a double bilayer system, simulating a cell membrane separating two different water compartments [49], resulting in a box containing two channels, 1184 lipids and a total of approximately 690 000 atoms. Before proceeding with the main trajectories, the pK_as of all titratable residues were calculated as done previously [50]. Briefly, short 10 ns unrestrained simulations were produced using the CHARMM36 force field, and frames were extracted at 2 ns intervals. The duration of these simulations was chosen to ensure adequate relaxation of ions, water molecules and partial side-chain movements while avoiding significant conformational changes of larger molecules. For each frame that was extracted, the PBEQ solver implemented in CHARMM [51] was used to calculate the pK_as. The calculated

average pKas were then used to determine the initial protonation states of titratable residues to mimic a pH environment of 7.4. After setting the residue protonation states, the system was minimized and equilibrated in six steps with decreasing restraints of the heavy atoms, for a total time of 1.5 ns. A first unrestrained simulation was then conducted for 100 ns. The structure obtained at 100 ns was then used for a second pKa calculation, aimed at identifying residues requiring a modification of their protonation state because of conformational changes of displacements of ions. After updating the residue protonation states, the system was again minimized and equilibrated in six steps with decreasing restraints on the heavy atoms, for a very short total time of 110 ps. Since the structure was extracted from an equilibrated MD simulation, the aim here was solely to allow for the surroundings of the modified sidechains to relax slightly before the simulation. This procedure was repeated five times until the completion of 500 ns (mutant) or 600 ns of simulation (WT).

(b) Multi-step computational determination of candidate residues interacting with the Ca^{2+} ions

Since classical MD reduces the complex electronic structure of atoms to simple spheres, our analysis did not aim to characterize the calcium electronic coordination *sensu stricto*. Coordination numbers or chelation modus were not investigated. Our project consisted of identifying negatively charged residues harbouring the most consistent interactions with the divalent ion, inferred through the comparison of duration of contact between the centre-of-mass of the carbonyl groups and the ion. We hypothesized that during a simulation, it is theoretically possible that a Ca^{2+} ion coordinated by a given ensemble of residues might leave this ensemble and get captured by another one. To avoid missing such new interactions, we conducted a two-step blind research of interacting pairs of Ca^{2+} ion–acidic residue. We observed that Ca^{2+} ions moved within the vestibule in which they were placed initially and, in some cases, left this vestibule (2 out of 12 Ca^{2+} ions placed in the WT and 5 out of 12 placed in the AP-Act mutant acidic pocket). If a Ca^{2+} ion that had left a vestibule appeared later in the simulation in a different vestibule, we did not include this second passage in the analysis, since the aim of the analysis was to monitor the interactions of the Ca^{2+} ion in the vestibule in which it was originally placed.

In the first step, the distances between all Ca^{2+} ions and all carbonyl groups were extracted at 10 ns intervals during each individual 100 ns long simulation. Since two proteins were simulated in the same box, this accounts for 2 (two proteins) × 18 (Ca^{2+}) × 183 (Glu and Asp) × 6 (individual 100 ns long simulations) × 10 (ten measurements during 100 ns) = 395280 distances. For the second step, any pair harbouring at least one occurrence with a Ca^{2+}-carbonyl group distance smaller than 10 Å was retained. These approximately 600 selected pairs were then subjected to the same distance calculation, but at intervals of 400 ps for a higher precision. To further isolate candidate residues, the distance threshold was reduced to 6 Å and residues were retained only if this distance criterion was met during at least 10% of the simulated time, i.e. during at least 10 ns during a 100 ns long trajectory. This second criterion did not require the interaction to be continuous in time.

(c) Molecular biology

The human ASIC1a clone (GenBank U78181 [52], in which the mutated residue Asp212 had been corrected to Gly [53]), rat ASIC1b-M3 (Genbank AJ30992; which was transcribed from the third Met, which corresponds to the first Met of ASIC1a [54]) and derived mutants were subcloned in the pSP65-derived vector pSD5 that contains 5′ and 3′ non-translated sequences of β-globin to improve the protein stability in *X. laevis* oocytes. Mutants were generated by site-directed mutagenesis using the QuikChange approach, with KAPA HiFi HotStart PCR polymerase (KAPA Biosystems, Roche). Combined mutants were synthesized by Genscript. Isolation of high-copy plasmid DNA from *Escherichia coli* was done using NucleoSpin Plasmid (MACHEREY-NAGEL). The mutations were verified by sequencing (Microsynth), and transcription was achieved using the mMESSAGE mMACHINE kit (Thermo Fisher Scientific).

(d) *Xenopus laevis* oocyte preparation and use

All animal experiments were carried out in accordance with Swiss laws and were approved by the veterinary service of the Canton de Vaud. In total, 1.3 g l^{-1} of MS-222 (Sigma-Aldrich) was used to anaesthetize female *X. laevis* frogs. The oocytes were extracted by a small incision on the abdominal wall, and the lobe was treated with 1 mg ml^{-1} collagenase for isolation and defolliculation. Healthy stage V and stage VI oocytes were selected. Oocytes were injected with 50 nl cRNA at 5–1100 ng μl^{-1}. Prior to electrophysiological measurements, the oocytes were stored in modified Barth's saline containing (in mM) 85 NaCl, 1 KCl, 2.4 $NaHCO_3$, 0.33 $Ca(NO3)_2$, 0.82 $MgSO_4$, 0.41 $CaCl_2$, 10 HEPES and 4.08 NaOH at 19°C.

It has been reported that lowering the extracellular Ca^{2+} concentration can induce inward currents in *X. laevis* oocytes owing to the activation of endogenous connexin hemichannels [55]. We have recently shown that a switch at pH 7.4 from a solution containing 2 mM Ca^{2+} to a solution containing 100 nM Ca^{2+} induces a slowly developing inward current in non-injected oocytes [18]. Owing to the small amplitude of this current, its effect on the pH_{50} of expressed ASICs was negligible. We have repeated these control experiments with oocyte batches used in the current study (electronic supplementary material, table S1 and figure S4). Decreasing the Ca^{2+} concentration from 2 mM/pH 7.4 to 100 nM produced an inward current of −54 ± 33 nA at a test pH 6.0 (n = 16; electronic supplementary material, figure S4*a*,*b*) and 1 ± 13 nA at test pH 7.4 (n = 16). Measurements at different pH conditions at the Ca^{2+} concentrations of 0.1 mM and 100 nM showed inward currents of the order of 100 nA or less (electronic supplementary material, figure S4*c* and table S1), suggesting that the presence of these low endogenous currents does not affect the pH dependence measurements of ASIC currents that were generally of several microamperes.

(e) Electrophysiological measurements

Electrophysiological recordings were performed 1–3 days after cRNA injection. Whole-cell currents were recorded by two-electrode voltage clamp using two glass electrodes filled with 1 M KCl with a resistance <0.5 MΩ. A Dagan TEV200 amplifier (Minneapolis, MN, USA), equipped with two bath electrodes, was used together with an InstruTECH LIH 8+8 interface and PatchMaster software (HEKA-Harvard Bioscience) to perform recordings. Current was recorded at a holding potential of −60 mV, at a sampling interval of 20 ms and filtered at 2 kHz. Oocytes were perfused with experimental solutions by gravity at a flow rate of 8–12 ml min^{-1}, using the cFLow 8 channel electro valve unit (Cell MicroControls) with an eightfold perfusion head. Measurements of the pH dependence or kinetics were done in paired experiments, comparing two divalent cation concentrations in the same oocyte. The recording solution contained (in mM) 110 NaCl, 10 HEPES for pH ≥ 6.8 and the indicated Ca^{2+} or Mg^{2+} concentration. HEPES was replaced by MES for solutions with a pH < 6.8 and by glycine for solutions with a pH ≤ 4. NaOH or HCl was used to adjust the pH. Solutions with <0.1 mM free Ca^{2+} or Mg^{2+} contained 10 mM EDTA for pH > 6.0 and 20 mM EDTA for pH ≤ 6. Total Ca^{2+} or Mg^{2+} concentrations were determined based on the MaxChelator program (https://somapp.ucdmc.ucdavis.edu/pharmacology/bers/maxchelator/webmaxc/webmaxcS.htm [56]) to obtain the desired free Ca^{2+} concentration. No chelator was added in solutions with ≥ 0.1 mM of Ca^{2+} or Mg^{2+}.

(f) Statistics and reproducibility

GraphPad Prism (v. 10) was used for the fits and the statistical analyses. For fitting the activation pH dependence, the Hill equation, $I = I_{max}/(1 + (10^{-pH\ 50}/10^{-pH})^{nH})$ was used, where I_{max} is the maximal current amplitude, pH_{50} is the pH inducing the half-maximal current amplitude and nH is the Hill coefficient; an analogous equation was used to fit the SSD pH dependence. The inhibition curves were fitted with the equation $I = NonIn+((I_{max}- NonIn)/(1 + (x_{Ca}/IC_{50})^{nH}))$, where NonIn is the non-inhibited current amplitude, I_{max} is the current amplitude at a free Ca^{2+} concentration of 0.1 mM, x_{Ca} is the Ca^{2+} concentration and nH is the Hill coefficient. The kinetics of recovery from desensitization were fitted to the equation $I = I_{max}\times (1 - e^{-t/\tau})$, where τ is the time constant and the other parameters are as defined above. The kinetics of SSD onset were fitted to the equation $I = NonDes + ((I_{max} - NonDes) \times e^{-t/\tau})$, where NonDes is non-desensitizing current. Statistical differences were analysed with one-way ANOVA test followed by a Dunnett's or Tukey's multiple comparisons test for comparison of ≥3 groups and a paired *t*-test for direct comparison of two groups. . Each experiment was done on at least two different days and with oocyte batches from at least two different frogs. Data are presented as individual data points or as mean ± s.d.

Ethics. All animal experiments were carried out in accordance with Swiss laws and were approved by the veterinary service of the Canton de Vaud, Licence VD1462.

Data accessibility. All experimental data are contained in the paper and electronic supplementary material [57]. No unique code was written to generate the data of this study.

Declaration of AI use. We have not used AI-assisted technologies in creating this article.

Authors' contributions. O.M.: conceptualization, investigation, methodology, visualization, writing—original draft, writing—review and editing; O.B.: conceptualization, investigation, methodology, visualization, writing—original draft, writing—review and editing; S.K.: conceptualization, funding acquisition, supervision, validation, visualization, writing—original draft, writing—review and editing.

All authors gave final approval for publication and agreed to be held accountable for the work performed therein.

Conflict of interest declaration. We declare we have no competing interests.

Funding. This work was supported by Swiss National Science Foundation grant 310030_207878 to S.K. This work was supported by computational resource grants from the Swiss National Supercomputing Centre (CSCS) under project IDs s1037 and s1099.

Acknowledgements. We thank Eleonora Centonze, Marc Bohnet and Mina Hanna for their comments on the manuscript.

References

1. Kellenberger S, Schild L. 2015 International union of basic and clinical pharmacology. XCI. Structure, function, and pharmacology of acid-sensing ion channels and the epithelial na+ channel. *Pharmacol. Rev.* **67**, 1–35. (doi:10.1124/pr.114.009225)
2. Wemmie JA, Taugher RJ, Kreple CJ. 2013 Acid-sensing ion channels in pain and disease. *Nat. Rev. Neurosci.* **14**, 461–471. (doi:10.1038/nrn3529)
3. Wemmie JA *et al*. 2002 The acid-activated ion channel ASIC contributes to synaptic plasticity, learning, and memory. *Neuron* **34**, 463–477. (doi:10.1016/s0896-6273(02)00661-x)
4. Jasti J, Furukawa H, Gonzales EB, Gouaux E. 2007 Structure of acid-sensing ion channel 1 at 1.9 Å resolution and low pH. *Nature* **449**, 316–323. (doi:10.1038/nature06163)
5. Sun D *et al*. 2020 Structural insights into human acid-sensing ion channel 1a inhibition by snake toxin mambalgin1. *eLife* **9**, e57096. (doi:10.7554/eLife.57096)
6. Baconguis I, Bohlen CJ, Goehring A, Julius D, Gouaux E. 2014 X-ray structure of acid-sensing ion channel 1-snake toxin complex reveals open state of a Na^+-selective channel. *Cell* **156**, 717–729. (doi:10.1016/j.cell.2014.01.011)
7. Kristián T, Siesjö BK. 1998 Calcium in ischemic cell death. *Stroke* **29**, 705–718. (doi:10.1161/01.str.29.3.705)
8. Formenti A, De Simoni A, Arrigoni E, Martina M. 2001 Changes in extracellular Ca^{2+} can affect the pattern of discharge in rat thalamic neurons. *J. Physiol.* **535**, 33–45. (doi:10.1111/j.1469-7793.2001.00033.x)
9. Rusakov DA, Fine A. 2003 Extracellular Ca^{2+} depletion contributes to fast activity-dependent modulation of synaptic transmission in the brain. *Neuron* **37**, 287–297. (doi:10.1016/s0896-6273(03)00025-4)
10. Hille B. 2001 *Ion channels of excitable membranes*, 3rd edn. Sunderland, MA: Sinauer Associates.
11. Chua HC, Wulf M, Weidling C, Rasmussen LP, Pless SA. 2020 The NALCN channel complex is voltage sensitive and directly modulated by extracellular calcium. *Sci. Adv.* **6**, eaaz3154. (doi:10.1126/sciadv.aaz3154)

12. Ma Z, Tanis JE, Taruno A, Foskett JK. 2016 Calcium homeostasis modulator (CALHM) ion channels. *Pflugers Arch.* **468**, 395–403. (doi:10.1007/s00424-015-1757-6)
13. Alijevic O, Peng Z, Kellenberger S. 2021 Changes in H^+, K^+, and Ca^{2+} concentrations, as observed in seizures, induce action potential signaling in cortical neurons by a mechanism that depends partially on acid-sensing ion channels. *Front. Cell. Neurosci.* **15**, 732869. (doi:10.3389/fncel.2021.732869)
14. Waldmann R, Champigny G, Bassilana F, Heurteaux C, Lazdunski M. 1997 A proton-gated cation channel involved in acid-sensing. *Nature* **386**, 173–177. (doi:10.1038/386173a0)
15. Babini E, Paukert M, Geisler HS, Grunder S. 2002 Alternative splicing and interaction with di- and polyvalent cations control the dynamic range of acid-sensing ion channel 1 (ASIC1). *J. Biol. Chem.* **277**, 41597–41603. (doi:10.1074/jbc.M205877200)
16. Immke DC, McCleskey EW. 2003 Protons open acid-sensing ion channels by catalyzing relief of Ca^{2+} blockade. *Neuron* **37**, 75–84. (doi:10.1016/s0896-6273(02)01130-3)
17. Paukert M, Babini E, Pusch M, Gründer S. 2004 Identification of the Ca^{2+} blocking site of acid-sensing ion channel (ASIC) 1: implications for channel gating. *J. Gen. Physiol.* **124**, 383–394. (doi:10.1085/jgp.200308973)
18. Roy S, Johner N, Trendafilov V, Gautschi I, Bignucolo O, Molton O, Bernèche S, Kellenberger S. 2022 Calcium regulates acid-sensing ion channel 3 activation by competing with protons in the channel pore and at an allosteric binding site. *Open Biol.* **12**, 220243. (doi:10.1098/rsob.220243)
19. Zuo Z, Smith RN, Chen Z, Agharkar AS, Snell HD, Huang R, Liu J, Gonzales EB. 2018 Identification of a unique Ca^{2+}-binding site in rat acid-sensing ion channel 3. *Nat. Commun.* **9**, 2082. (doi:10.1038/s41467-018-04424-0)
20. Yoder N, Gouaux E. 2018 Divalent cation and chloride ion sites of chicken acid sensing ion channel 1a elucidated by x-ray crystallography. *PLoS ONE* **13**, e0202134. (doi:10.1371/journal.pone.0202134)
21. Paukert M, Chen X, Polleichtner G, Schindelin H, Gründer S. 2008 Candidate amino acids involved in H^+ gating of acid-sensing ion channel 1a. *J. Biol. Chem.* **283**, 572–581. (doi:10.1074/jbc.M706811200)
22. Krauson AJ, Rued AC, Carattino MD. 2013 Independent contribution of extracellular proton binding sites to ASIC1a activation. *J. Biol. Chem.* **288**, 34375–34383. (doi:10.1074/jbc.M113.504324)
23. Krauson AJ, Carattino MD. 2016 The thumb domain mediates acid-sensing ion channel desensitization. *J. Biol. Chem.* **291**, 11407–11419. (doi:10.1074/jbc.M115.702316)
24. Sherwood T, Franke R, Conneely S, Joyner J, Arumugan P, Askwith C. 2009 Identification of protein domains that control proton and calcium sensitivity of ASIC1a. *J. Biol. Chem.* **284**, 27899–27907. (doi:10.1074/jbc.M109.029009)
25. Liechti LA, Bernèche S, Bargeton B, Iwaszkiewicz J, Roy S, Michielin O, Kellenberger S. 2010 A combined computational and functional approach identifies new residues involved in pH-dependent gating of ASIC1a. *J. Biol. Chem.* **285**, 16315–16329. (doi:10.1074/jbc.M109.092015)
26. Yoder N, Yoshioka C, Gouaux E. 2018 Gating mechanisms of acid-sensing ion channels. *Nature* **555**, 397–401. (doi:10.1038/nature25782)
27. Vullo S, Bonifacio G, Roy S, Johner N, Bernèche S, Kellenberger S. 2017 Conformational dynamics and role of the acidic pocket in ASIC pH-dependent gating. *Proc. Natl Acad. Sci. USA* **114**, 3768–3773. (doi:10.1073/pnas.1620560114)
28. Vullo S, Ambrosio N, Kucera JP, Bignucolo O, Kellenberger S. 2021 Kinetic analysis of ASIC1a delineates conformational signaling from proton-sensing domains to the channel gate. *eLife* **10**, e66488. (doi:10.7554/eLife.66488)
29. Bonifacio G, Lelli CIS, Kellenberger S. 2014 Protonation controls ASIC1a activity via coordinated movements in multiple domains. *J. Gen. Physiol.* **143**, 105–118. (doi:10.1085/jgp.201311053)
30. Passero CJ, Okumura S, Carattino MD. 2009 Conformational changes associated with proton-dependent gating of ASIC1a. *J. Biol. Chem.* **284**, 36473–36481. (doi:10.1074/jbc.M109.055418)
31. Roy S, Boiteux C, Alijevic O, Liang C, Bernèche S, Kellenberger S. 2013 Molecular determinants of desensitization in an ENaC/degenerin channel. *FASEB J.* **27**, 5034–5045. (doi:10.1096/fj.13-230680)
32. Bässler EL, Ngo-Anh TJ, Geisler HS, Ruppersberg JP, Gründer S. 2001 Molecular and functional characterization of acid-sensing ion channel (ASIC) 1b. *J. Biol. Chem.* **276**, 33782–33787. (doi:10.1074/jbc.M104030200)
33. Immke DC, McCleskey EW. 2001 Lactate enhances the acid-sensing Na^+ channel on ischemia-sensing neurons. *Nat. Neurosci.* **4**, 869–870. (doi:10.1038/nn0901-869)
34. Gröber U, Schmidt J, Kisters K. 2015 Magnesium in prevention and therapy. *Nutrients* **7**, 8199–8226. (doi:10.3390/nu7095388)
35. Sen AP, Gulati A. 2010 Use of magnesium in traumatic brain injury. *Neurotherapeutics* **7**, 91–99. (doi:10.1016/j.nurt.2009.10.014)
36. Bindreither D, Lackner P. 2009 Structural diversity of calcium binding sites. *Gen. Physiol. Biophys.* **28**, F82–F88.
37. Pless SA, Ahern CA. 2013 Unnatural amino acids as probes of ligand-receptor interactions and their conformational consequences. *Annu. Rev. Pharmacol. Toxicol.* **53**, 211–229. (doi:10.1146/annurev-pharmtox-011112-140343)
38. Denesyuk AI, Permyakov SE, Johnson MS, Denessiouk K, Permyakov EA. 2020 System approach for building of calcium-binding sites in proteins. *Biomolecules* **10**, 588. (doi:10.3390/biom10040588)
39. Nara M, Morii H, Tanokura M. 2013 Coordination to divalent cations by calcium-binding proteins studied by FTIR spectroscopy. *Biochim. Biophys. Acta* **1828**, 2319–2327, (doi:10.1016/j.bbamem.2012.11.025)
40. Mayer ML, Westbrook GL, Guthrie PB. 1984 Voltage-dependent block by Mg2+ of NMDA responses in spinal cord neurones. *Nature* **309**, 261–263. (doi:10.1038/309261a0)
41. Zhang P, Sigworth FJ, Canessa CM. 2006 Gating of acid-sensitive ion channel-1: release of Ca^{2+} block vs. allosteric mechanism. *J. Gen. Physiol.* **127**, 109–117. (doi:10.1085/jgp.200509396)
42. Gonzales EB, Kawate T, Gouaux E. 2009 Pore architecture and ion sites in acid-sensing ion channels and P2X receptors. *Nature* **460**, 599–604. (doi:10.1038/nature08218)
43. Baconguis I, Gouaux E. 2012 Structural plasticity and dynamic selectivity of acid-sensing ion channel-spider toxin complexes. *Nature* **489**, 400–405. (doi:10.1038/nature11375)
44. Wang X, Kirberger M, Qiu FS, Chen GT, Yang JJ. 2009 Towards predicting Ca^{2+}-binding sites with different coordination numbers in proteins with atomic resolution. *Proteins* **75**, 787–798. (doi:10.1002/prot.22285)
45. Geng Y *et al*. 2016 Structural mechanism of ligand activation in human calcium-sensing receptor. *eLife* **5**, e13662. (doi:10.7554/eLife.13662)
46. Biasini M *et al*. 2014 SWISS-MODEL: modelling protein tertiary and quaternary structure using evolutionary information. *Nucleic Acids Res.* **42**, W252–W258. (doi:10.1093/nar/gku340)
47. Yoder N, Gouaux E. 2020 The His-Gly motif of acid-sensing ion channels resides in a reentrant 'loop' implicated in gating and ion selectivity. *eLife* **9**, e56527. (doi:10.7554/eLife.56527)
48. Jorgensen WL, Chandrasekhar J, Madura JD, Impey RW, Klein ML. 1983 Comparison of simple potential functions for simulating liquid water. *J. Chem. Phys.* **79**, 926–935. (doi:10.1063/1.445869)
49. Bignucolo O, Bernèche S. 2020 The voltage-dependent deactivation of the KvAP channel involves the breakage of its S4 helix. *Front. Mol. Biosci.* **7**, 162. (doi:10.3389/fmolb.2020.00162)

50. Bignucolo O, Chipot C, Kellenberger S, Roux B. 2022 Galvani offset potential and constant-pH simulations of membrane proteins. *J. Phys. Chem. B* **126**, 6868–6877. (doi:10.1021/acs.jpcb.2c04593)
51. Jo S, Vargyas M, Vasko-Szedlar J, Roux B, Im W. 2008 PBEQ-Solver for online visualization of electrostatic potential of biomolecules. *Nucleic Acids Res.* **36**, W270–W275. (doi:10.1093/nar/gkn314)
52. García-Añoveros J, Derfler B, Neville-Golden J, Hyman BT, Corey DP. 1997 BNaC1 and BNaC2 constitute a new family of human neuronal sodium channels related to degenerins and epithelial sodium channels. *Proc. Natl Acad. Sci. USA* **94**, 1459–1464. (doi:10.1073/pnas.94.4.1459)
53. Vaithia A, Vullo S, Peng Z, Alijevic O, Kellenberger S. 2019 Accelerated current decay kinetics of a rare human acid-sensing ion channel 1a variant that is used in many studies as wild type. *Front. Mol. Neurosci.* **12**, 133. (doi:10.3389/fnmol.2019.00133)
54. Bässler EL, Ngo-Anh TJ, Geisler HS, Ruppersberg JP, Gründer S. 2001 Molecular and functional characterization of acid-sensing ion channel (ASIC) 1b. *J. Biol. Chem*. **276**, 33782–33787. (doi:10.1074/jbc.M104030200)
55. Ebihara L. 1996 *Xenopus* connexin38 forms hemi-gap-junctional channels in the nonjunctional plasma membrane of *Xenopus* oocytes. *Biophys. J*. **71**, 742–748. (doi:10.1016/S0006-3495(96)79273-1)
56. Bers DM, Patton CW, Nuccitelli R. 2010 A practical guide to the preparation of Ca^{2+} buffers. *Methods Cell Biol*. **99**, 1–26. (doi:10.1016/B978-0-12-374841-6.00001-3)
57. Molton O, Bignucolo O, Kellenberger S. 2024 Identification of the modulatory Ca^{2+} binding sites of acid-sensing ion channel 1a. *Figshare*. (doi:10.6084/m9.figshare.c.7227186)